Measurement of the Total Electron-Hydrogen Scattering Cross Section for the Project 8 Experiment

by

Devyn Marie Rysewyk

Submitted to the Department of Physics
in partial fulfillment of the requirements for the degree of

Bachelor of Science in Physics

at the

MASSACHUSETTS INSTITUTE OF TECHNOLOGY

June 2015

Author .... Signature redacted ....
Department of Physics
May 8, 2015

Certified by .... Signature redacted ....
Professor Joseph Formaggio
Thesis Supervisor, Department of Physics

Accepted by .... Signature redacted ....
Professor Nergis Mavalvala
Senior Thesis Coordinator, Department of Physics

Measurement of the Total Electron-Hydrogen Scattering Cross Section for the Project 8 Experiment

by

Devyn Marie Rysewyk

Submitted to the Department of Physics
on May 8, 2015, in partial fulfillment of the
requirements for the degree of
Bachelor of Science in Physics

Abstract

Project 8 is an experiment that aims to determine the neutrino mass from a measurement of the endpoint of the tritium beta-decay continuous energy distribution. To do this, Project 8 is utilizing the cyclotron radiation of electrons in a magnetic field. In June 2014, Project 8 saw the first cyclotron radiation signals from single electrons. The frequency spectrum showed that there are frequency jumps between each track. Using the simulation package, Kassiopeia, data collected on June 2014 were compared against Monte Carlo scattering predictions. This thesis presents the analysis of these frequency jumps. This thesis also presents electron-hydrogen cross section values for the simulations and theoretical models. The cross section for the simulations is used to approximate the number density of the experiment.

Thesis Supervisor: Professor Joseph Formaggio
Title: Thesis Supervisor, Department of Physics

Acknowledgments

I would like express my sincere thanks to Professor Joseph Formaggio and Dr. Noah Oblath for being my mentors for the past four years. I would also like to thank my family and friends for the continued support and encouragement throughout my time at MIT.

Contents

1 Theory of Beta-Decay **9**

1.1 Introduction 9

1.2 Theory 11

2 Project 8 Experiment **13**

2.1 Magnetic and Waveguide Systems 13

2.2 Gas and Vacuum Systems 16

2.3 Detection and Analysis of the Electrons 17

3 Scattering Cross Section **21**

3.1 Attenuation Time 21

3.2 From Rutherford to Binary-Encounter Models 23

3.2.1 Rutherford Scattering 23

3.2.2 Mott Scattering 23

3.2.3 Binary-Encounter Dipole Model 24

3.3 Hydrogen Scattering 26

3.3.1 Total Scattering Cross Section 26

3.3.2 Energy Loss 28

4 Description of the Data and Simulations **29**

4.1 Data Set 29

4.2 Conditions on Tracks and Events 30

4.3 Simulations 31

5 Track Length Analysis **35**

5.1 Data 35

5.2 Simulation 38

5.3 Results 40

6 Frequency Jump Analysis **45**

6.1 Data 45

6.2 Simulations 46

6.3 Results 53

7 Conclusions **59**

Chapter 1

Theory of Beta-Decay

1.1 Introduction

Neutrinos have been particularly mysterious particles ever since their discovery, and the experiments leading up to the discovery of neutrinos were no different. When James Chadwick was investigating β-decay in 1912, he discovered something rather surprising [1]. Earlier, he observed discrete lines in the energy spectrum for α-decay and γ-decay. However, when he investigated β-decay, he observed a continuous energy spectrum, which seemed to violate energy conservation laws. To look more into this phenomenon, calorimetric measurements were executed by C.D. Ellis in 1927 and L. Meitner in 1930 [1]. Both Ellis and Meitner confirmed the primary origin of the continuous energy spectrum for β-decay; therefore, Wolfgang Pauli wrote his famous letter in December of 1930 proposing a new particle that solved the conservation law problem [1]. This particle, that we now call the neutrino, would be a spin-$\frac{1}{2}$, light, and neutral particle. It would be an additional 20 years before neutrinos were actually observed and discovered.

The first experimental evidence of neutrinos was during a nuclear recoil experiment conducted by Rodeback and Allen in 1952 [2]; however, it was during an experiment in 1956 where neutrinos were first detected and observed. Clyde Cowan and Frederick

Reines designed their experiment to detect inverse beta decay [3]:

$$\bar{\nu}_e + p \rightarrow n + e^+ \tag{1.1}$$

They built their initial experiment in 1953 in Hanford; however they later moved it underground at the Savannah River reactor because they experienced too much noise from cosmic rays. Moving the experiment underground proved successful when they observed inverse beta decay in 1956, and therefore detecting neutrinos [3]. Since then, there have been many experiments with neutrinos, including experiments that resulted in the discovery of the three flavors of neutrinos (ν_e, ν_μ, and ν_τ) and neutrino oscillations.

Currently, there are several experiments that aim to directly measure the mass of the neutrino, for which the scale to this day remains unknown. These experiments include KATRIN, HOLMES, ECHO, and Project 8 [4, 10, 12, 11, 13].

Project 8 is an experiment being developed to measure the neutrino mass, which is determined by measuring the frequency of electrons that are being emitted from the β-decay of tritium. Tritium decays over time, and each decay releases an electron and an antineutrino:

$$^3\mathrm{H} \rightarrow \; ^3\mathrm{He} + e^- + \bar{\nu}_e \tag{1.2}$$

Since the β-decay energy distribution depends on whether the neutrino is massive or not, a measurement of this distribution is equivalent to a neutrino mass measurement. An example of the distribution and the effect of the mass of a neutrino on the distribution is shown in Fig. 1-1.

To measure the energies of the electrons that are emitted in the β-decay of tritium, Project 8 will measure the cyclotron frequency of the emitted electrons in a uniform magnetic field. This magnetic field is created by a superconducting solenoid. The current Project 8 experiment is located in the Physics and Astronomy Building at the University of Washington in Seattle.

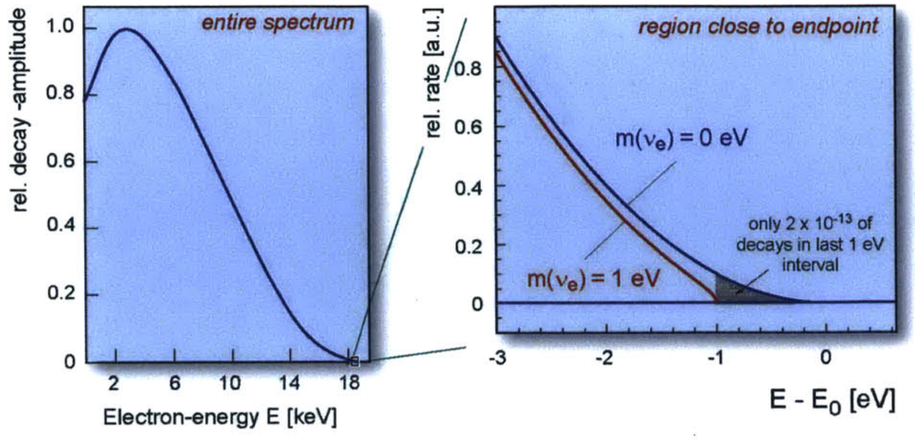

Figure 1-1: The continuous energy distribution and the effect the neutrino has on the endpoint of the spectrum.

1.2 Theory

As mentioned in Section 1.1, Project 8 will measure the frequency of electrons emitted in the beta-decay of tritium. Frequency measurements allow extremely precise investigations into physical quantities. In particular, Project 8 will extract the cyclotron frequency of electrons inside of a uniform magnetic field. The relativistic cyclotron frequency can be calculated as follows [6]:

$$f_\gamma = \frac{ec^2 B}{2\pi(m_e c^2 + K)} \tag{1.3}$$

where e is the charge of the electron, c is the speed of light, B is the magnetic field, m_e is the mass of the electron, and K is the kinetic energy of the electron. Because Eq. 1.3 relates the cyclotron frequency and the kinetic energy of the electron, the energy can be calculated in a non-destructive way [6].

Electrons that accelerate inside of a magnetic field radiate. The radiation generated by moving electrons in a magnetic field can be used to make the frequency measurement. However, because Project 8 measures the cyclotron frequency of single electrons, the signal from the radiation is very small. The total power radiated is given by [5]:

$$P = \frac{e^4 B^2}{6\pi\varepsilon_0 m_e^4 c^5}(K^2 + 2m_e c^2 K) sin^2\theta \tag{1.4}$$

where ε_0 is the permittivity of free space and θ is the angle between the momentum vector of the electron and the magnetic field. For an 18.6 keV electron (the energy near the endpoint of the tritium β-decay distribution) in a 1 T field with a θ of 90°, the total power radiated is around 1.2 fW [6]. In order to measure a signal this small, Project 8 will need to detect the signal over a long period of time. How this is achieved will be discussed in Section 2.1. The electrons also undergo radiation loss and scattering which will affect the data.

Chapter 2

Project 8 Experiment

To make Project 8 become realizable, it requires a magnetic field for the electrons to accelerate through, a radioactive gas source of the electrons, and a RF antenna system to receive the cyclotron radiation signals.

2.1 Magnetic and Waveguide Systems

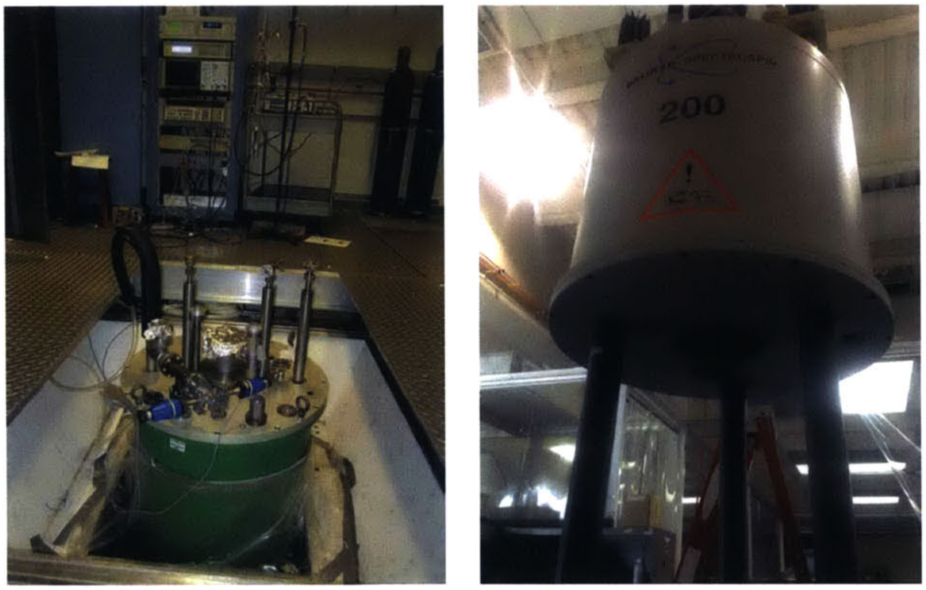

Figure 2-1: The cold-bore solenoidal magnet is shown on the left and the current warm-bore NMR magnet is shown on the right [5].

To achieve a uniform magnetic field, Project 8 utilizes large superconducting solenoids to produce the magnetic field. During the prototype stage, Project 8 used a cold-bore solenoidal magnet. This magnet contained X, Y, Z, and Z^2 shim coils that corrected the magnetic field of the main coil to make it more uniform. The cold-bore solenoidal magnet was capable of magnetic fields up to 6 Tesla. Currently, Project 8 uses a warm-bore Bruker-Spectrospin 200 MHz NMR magnet. The NMR magnet is capable of creating magnetic fields up to 4.7 Tesla. Both magnets are shown in Fig. 2-1.

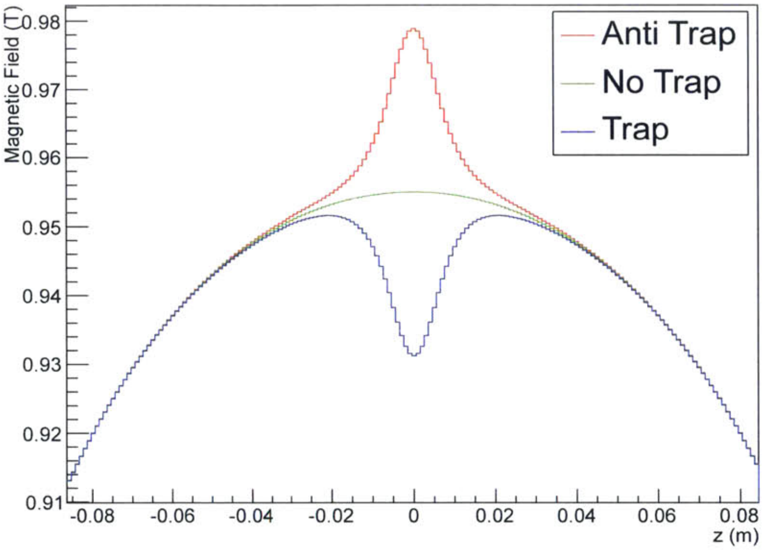

Figure 2-2: An example of the main magnetic field is shown in green. When the trap coil is turned on with the opposite polarity as the main magnet, the overall magnetic field has a dip in the center, which is shown in blue. The overall magnet field shown in red is when the trap coil and the main magnet have the same polarity.

In order to have enough time to make a precise frequency measurement, Project 8 has a coil that is located in the center of the NMR magnet. This coil is known as the trap coil. When the experiment is running, the magnetic field produced by the trap coil is of opposite polarity than the magnetic field produced by the NMR magnet. This creates a dip in the center of the overall magnetic field, which can be seen in Fig. 2-2. When the electrons are emitted inside of this dip, most of the electrons will escape. However, a few electrons will be trapped. Specifically, the electrons whose momentum vector is near perpendicular to the direction of the magnetic field will be trapped inside of the dip. An example of a simulation that shows the trap coil and the trapped particle is shown in Fig. 2-3. We can observe the trapped electrons long enough to detect a signal. Another type of trap that Project 8 will investigate is the bathtub-like trap. This configuration contains two coils that are equally spaced from the center of the magnet. These coils, which have the same polarity as the main magnet, create two sharp peaks in the magnetic field with a relatively flat field in between, forming a bath-tub like magnetic field. An example can be seen in Fig. 2-4.

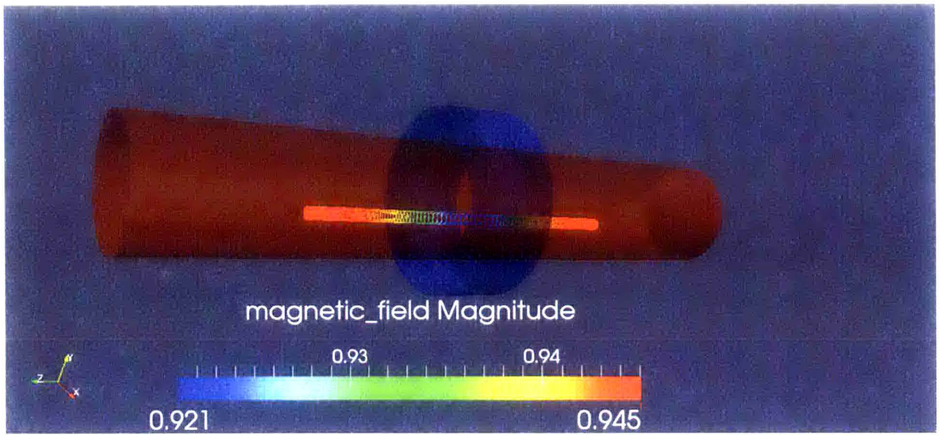

Figure 2-3: A simulation of a trapped electron inside the waveguide. The electron was created with a momentum vector near perpendicular to the magnetic field in order to ensure that it was trapped.

Since the cyclotron frequency is dependent on the strength of the magnetic field, as seen in Eq. 1.3, we must have a precise measurement of the magnetic field. To do this, Project 8 utilizes the organic chemical compound 2,2-diphenyl-1-picrylhydrazyl (DPPH). DPPH is a dark crystalline powder that contains a near-free electron. When placed in a magnetic field, the DPPH has an extremely sharp, strong resonance line [7]. For Project 8, a vial of DPPH is placed inside a WR42 waveguide. The waveguide is placed inside the magnet with the trap coil wrapped around it, aligned with the center axis of the magnet. With the DPPH and other calibration methods, Project 8 is able to have a very precise measurement of the magnetic field. For the data run conducted on June 27, 2014, the magnetic field of the NMR magnet was measured to be 0.94542 ± 0.00024 Tesla.

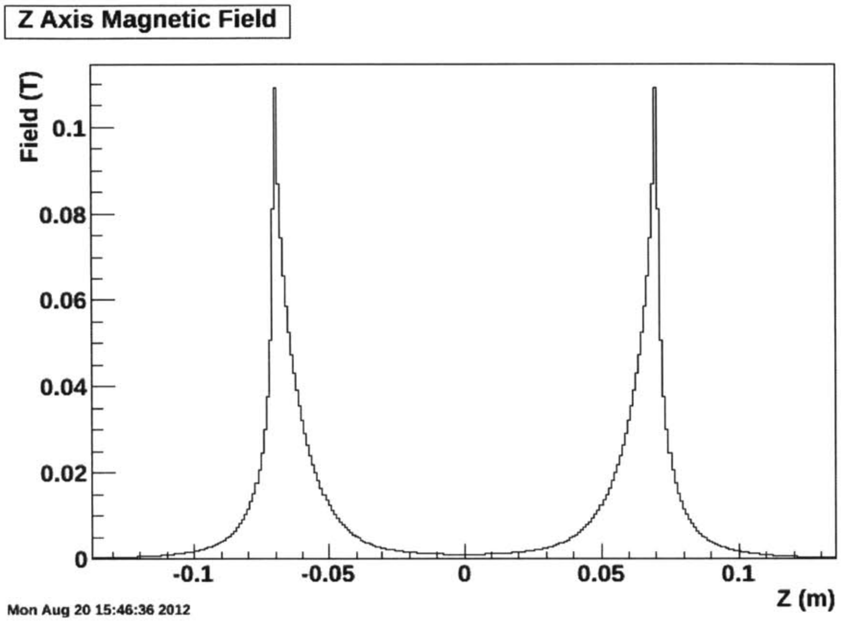

Figure 2-4: An example of a bathtub-like magnetic trap. The trap is created by two small coils with the same polarity. These coils are placed on opposite sides but an equal distance from the center.

2.2 Gas and Vacuum Systems

The gas system for Project 8 is needed because ^{83}Rb is being utilized as the source of the electrons. ^{83}Rb, which has a half-life of around 86 days, decays to ^{83m}Kr. ^{83m}Kr then decays to ^{83}Kr with a half-life of 1.8 hours. Conversion electrons are emitted in the decay from ^{83m}Kr to ^{83}Kr. These conversion electrons have energies of 17.8, 30.4, and 32 keV. There are no neutrinos emitted in this process. Project 8 is using ^{83}Rb in order to prove that we are able to observe and measure the cyclotron frequency of a single electron before moving to the ^{3}H experiment. The rubidium is contained in zeolite beads, and when the rubidium decays into krypton, the krypton escapes the beads and enters the gas system [5].

Because gas is present in the experiment, Project 8 also uses a vacuum system. The vacuum system is used to decrease the amount of gases other than krypton inside of the system. Theoretically, we only want krypton in the gas system during data-taking because having any other gases in the system can induce scattering. Scattering would greatly decrease the length a particle travels inside the waveguide.

The vacuum system contains a turbo pump that removes noble gases in the system down to a pressure of about 10^{-8} mbar [5]. A nonevaporable getter pump is also used in conjunction with the turbo pump to remove the non-noble gas load. The turbo pump is then turned off and the krypton enters the gas system.

2.3 Detection and Analysis of the Electrons

The conversion electrons that are created inside the waveguide emit cyclotron radiation. Most of the electrons escape out of the waveguide quickly; however, some of them remain in the waveguide for a few milliseconds. An example of the cyclotron motion a trapped electron undergoes is shown in Fig. 2-3.

Once the electrons exit the waveguide, their signals travel to two low-noise amplifiers placed in series. The first stage amplifies the signal between 25 GHz and 27 GHz. These frequencies are then mixed with a local oscillator at 24.2 GHz down to a center frequency of 1.8 GHz [6]. The signal is amplified and then travels to the second stage, where the signal is mixed down to 100 MHz band. Here the signal is again amplified and sent to the computer by an 8-bit digitizer.

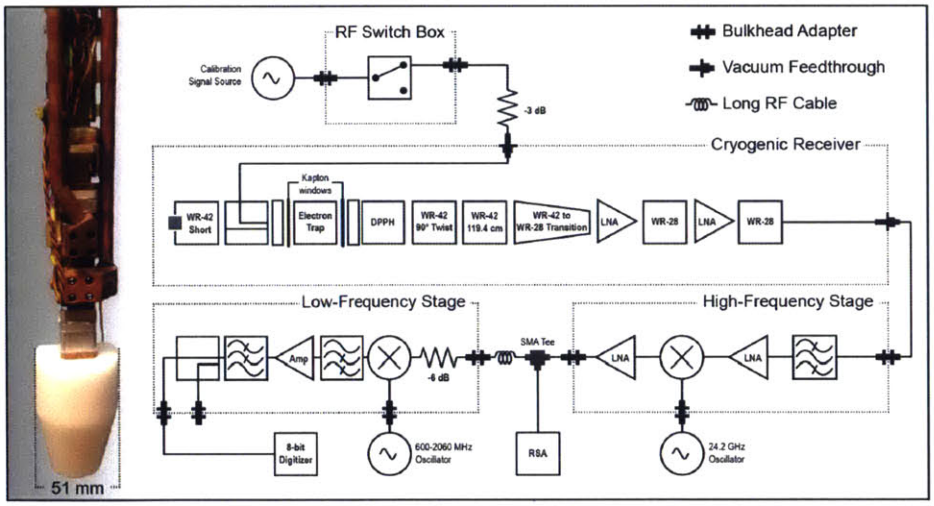

Figure 2-5: The waveguide and gas lines are shown on the left. The receiver chain is shown on the right. It consists of the cryogenic receiver and the two stage amplifying system before the signal is sent through the digitizer to the computer for data acquisition and analysis [6].

The data is collected through a program called Mantis. The data is acquired and then sent out to participating institutions for analysis. There are currently many sets of analyses being conducted by the different institutions on Project 8. One of the analyses focuses on using the Fast Fourier Transform (FFT) which uses the Discrete Fourier Transform (DFT). The basic idea of a Fourier transform is to represent a wave form in terms of frequency instead of time [8]. The Fourier Transform can be defined as [8]:

$$g(\xi) = \sum_{n=\infty}^{\infty} c_n e^{2\pi inx/P} \tag{2.1}$$

where x is time, P is the period, and c_n are the coefficients of the Fourier Transform, which are defined by:

$$c_n = \frac{1}{P}\int_0^P g(x)e^{-2\pi inx/P}dx \tag{2.2}$$

In order to derive the DFT, we have to consider the k^{th} coefficient. The left-endpoint, uniform Riemann sum is used to approximate the integral with the result of:

$$c_k \approx \frac{1}{N}\sum_{j=0}^{N-1} g\left(j\frac{P}{N}\right) e^{-2\pi ijk/N}dx \tag{2.3}$$

This Riemann approximation drives the definition of the N-point DFT [8]:

$$H_k = \sum_{j=0}^{N-1} h_j e^{-2\pi ijk/N} \tag{2.4}$$

where k is any integer.

Project 8 uses the Fastest Fourier Transform in the West's (FFTW) library to compute the DFT [9]. Once the data is run through the DFT, we square the result to obtain the power. The data is then cut into slices, where each slice is plotted into a power versus frequency histogram. The noise in each histogram is fit with a spline function, and then multiplied to get the threshold. The threshold is then cut from the histogram and only the high power bins remain. This is done for each slice of data, and then all of the slices are put into a frequency versus time graph. The power slices are arranged in order by time. This graph is run through a Density-Based Spatial

Clustering of Applications with Noise (DBSCAN) algorithm to find clusters of high power bins. Once the algorithm finds a cluster, a least squares fit is fit to the cluster to give a track. The tracks are then put into another frequency versus time graph. Another DBSCAN is run for the tracks, except it is altered to run from the end of one track to the beginning of another. The DBSCAN allows relatively any difference in frequency, but only a small difference in time. The tracks that are close in time will create events. With this analysis, Project 8 has found many events in data that was taken in June 2014. An example of an event is shown in Fig. 2-6.

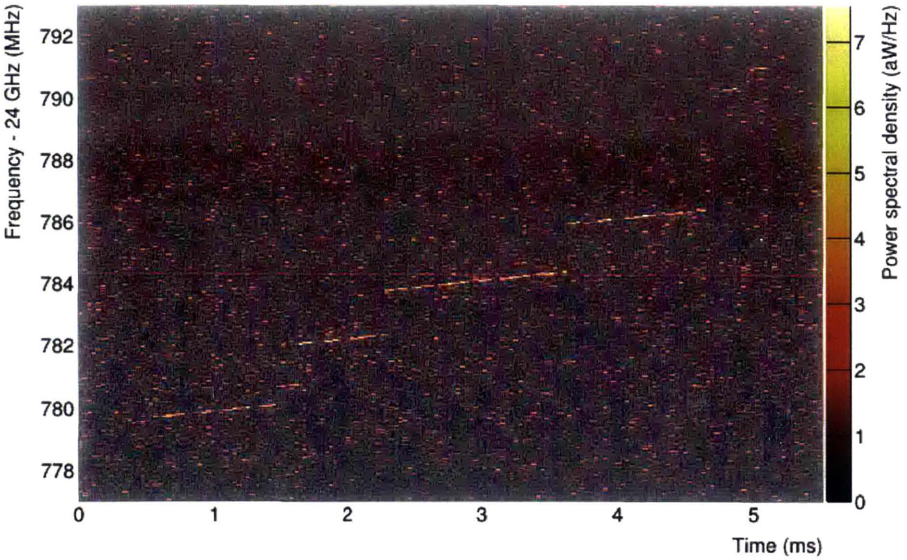

Figure 2-6: An example of an event in the experiment [6].

The event in Fig. 2-6 started with an electron that had a kinetic energy of 30.4 keV. The electron increases in frequency as it accelerates in the magnetic field and loses energy due to cyclotron radiation. The electron also has sharp frequency jumps that are caused by scattering with the hydrogen gas in the experiment. When these electrons scatter, their energy and pitch-angle change; therefore giving a jump in frequency and a drop in energy. These drops in energy will be analyzed in Section 6.2.

Chapter 3

Scattering Cross Section

3.1 Attenuation Time

Scattering occurs when an incident particle collides with a target particle. The initial properties of the incident particle, such as the initial frequency and the initial angle, will change upon scattering. A simple representation of scattering can be seen in Fig. 3-1. The scattering cross section is defined as the effective area of collision. The probability of collision can be defined as [20]:

$$dP = \sigma n dx \tag{3.1}$$

where σ is the scattering cross section and n is the density of target particles. The number of particles, N, that survive after traveling a distance, x, in a region with a target particle density, n, and scattering cross section, σ, is given by [20]:

$$N(x) = N_{x_0} e^{-\sigma n x} \tag{3.2}$$

where the attenuation length μ_l can be defined as:

$$\mu_l = \sigma n \tag{3.3}$$

where μ_l has units of m^{-1}.

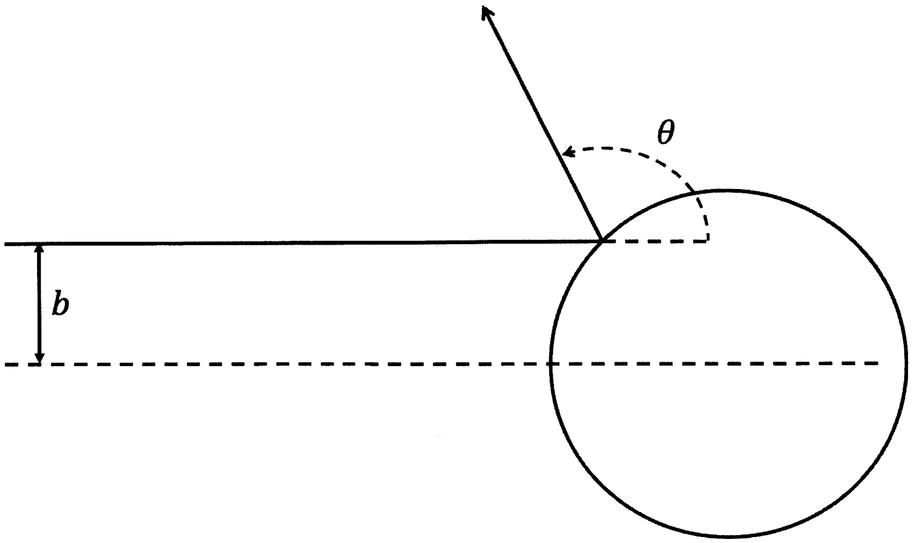

Figure 3-1: An example of hard sphere scattering. A particle with an impact parameter, b, collides with a hard sphere and scatters off in a different direction.

For the Project 8 experiment, only the time that the particle survived before scattering or exiting the experiment can be extracted. This is called the track time. The track time will have the form of a decaying exponential similar to Eq. 3.2:

$$N(t) = N_{t_0} e^{-\mu_t t} \tag{3.4}$$

where μ_t is the attenuation time with units s^{-1}. In order to represent μ_t in terms of σ and n, the velocity of the particles must be known. From special relativity, the kinetic energy of a particle that is traveling near the speed of light can be defined as:

$$K = (\gamma - 1) m_e c^2 \tag{3.5}$$

where $\gamma = 1/\sqrt{1-\beta^2}$ and $\beta = v/c$. Electrons with energies of 17.8 keV, 30.4 keV, and 32.0 keV have β-factors of $\beta_{17.8} = .2573$, $\beta_{30.4} = .3304$, and $\beta_{32.0} = .3382$. These electrons are considered relativistic. By manipulating Eq. 3.5, μ_t can be represented by:

$$\mu_t = \sigma n v = \sigma n c \sqrt{1 - \frac{m_e^2 c^4}{(K + m_e c^2)^2}} \tag{3.6}$$

3.2 From Rutherford to Binary-Encounter Models

3.2.1 Rutherford Scattering

In the early 1900s, Hans Geiger and Ernest Marsden performed experiments that aimed α-particles at metal foils with varying thicknesses. At the time, the accepted model of the atom was the plum pudding model. This model was proposed by J.J. Thompson in 1904. The plum pudding model suggests that the atom was a positively charged body with free-floating, negatively charged particles inside. Geiger and Marsden produced results that were contradictory to this model; in particular, that some of the α-particles had extremely large scattering angles. This led Ernest Rutherford to propose a new structure of the atom in 1911 [21]. Rutherford's model suggests that electrons orbit around a massive, positively-charged nucleus. This also led to Rutherford Scattering, where scattered particles are nonrelativistic and the target recoil is neglected.

The scattering between a particle with charge $Z_1 e$ (where Z_1 is the atomic number of the atom) and a free electron that is at rest has the differential cross section of [19]:

$$\frac{d\sigma(W,T)}{dW} = \frac{4\pi a_0^2 Z_1^2 R^2}{T}\frac{1}{W^2} \tag{3.7}$$

where a_0 is the Bohr radius, R is the Rydberg energy, T is the reduced kinetic energy $T = m_e v^2/2$, m_e is the mass of an electron, v is the relative velocity, and W is the kinetic energy of the ejected electron.

3.2.2 Mott Scattering

Mott Scattering is similar to Rutherford scattering, except that Mott is relativistic and Rutherford is not. The Mott cross section is for the scattering of two free electrons is [19]:

$$\frac{d\sigma(W,T)}{dW} = \frac{4\pi a_0^2 R^2}{T}\left[\frac{1}{W^2} - \frac{1}{W(T-W)} + \frac{1}{(T-W)^2}\right] \tag{3.8}$$

where T is the kinetic energy of the incident electron and $T-W$ is the kinetic energy of the scattered electron.

The Mott cross section can be further modified to consider a bound electron in an atom. W is replaced with the energy transfer, $E=W+B$, where B is the binding energy of the ejected electron [19]. T is also replaced with $T+B$. Taking in these two differences, the modified Mott cross section for a subshell becomes [19]:

$$\frac{d\sigma(W,T)}{dW}=\frac{d\sigma}{dE}=\frac{4\pi a_0^2R^2N}{T}\left[\frac{1}{E^2}-\frac{1}{E(T-W)}+\frac{1}{(T-W)^2}\right] \tag{3.9}$$

where N is the number of bound electrons in the subshell.

3.2.3 Binary-Encounter Dipole Model

The Binary-Encounter Dipole (BED) Model is an extension of the Mott cross section. The BED Model also describes the ionization of the bound target electron and adds a velocity or momentum distribution to the bound electron. This takes into account the motion of the bound electron around the nucleus [19]. The Binary-Encounter cross section can be expressed as [19]:

$$\begin{aligned}\frac{d\sigma(E,T)}{dE}=\frac{4\pi a_0^2R^2N}{T+U+B}\Bigg\{&\frac{1}{E^2}-\frac{1}{E(T-W)}+\frac{1}{(T-W)^2}\\&+\frac{4U}{3}\left[\frac{1}{E^3}+\frac{1}{(T-W)^3}\right]\Bigg\}\end{aligned} \tag{3.10}$$

where U is the average kinetic energy of the electrons in the subshell. U is defined as [19]:

$$U\equiv\frac{\langle\overrightarrow{p}\rangle}{2m} \tag{3.11}$$

where $\overrightarrow{p}$ is the momentum operator of the electrons in the subshell.

The variables of Eq. 3.10 can be written in terms of the binding energy of the electron: $t=T/B$, $w=W/B$, $u=U/B$, and $S=4\pi a_0^2N(R/B)^2$. With these definitions, the BED cross section can be written as [19]:

$$\frac{d\sigma(W,T)}{dW} = \frac{S}{B}\sum_{n=1}^{3} F_n(t)\left[\frac{1}{(w+1)^n} + \frac{1}{(t-w)^n}\right] \tag{3.12}$$

where $F_n(t)$ are [19]:

$$F_1 = -\frac{F_2}{t+1}, F_2 = \frac{1}{t+u+1}, F_3 = \frac{4u}{3(t+u+1)} \tag{3.13}$$

However, the asymptotic behavior of the total ionization cross section that is calculated from Eq. 3.12 does not agree with the Bethe theory which describes the energy loss due to ionization. In order to produce dependable cross section results for ionization, the BED model must be modified to [19]:

$$\begin{aligned}\frac{d\sigma(W,T)}{dW} = \frac{S}{B(t+u+1)}&\left\{\frac{(N_i/N)-2}{t+1}\left(\frac{1}{w+1}+\frac{1}{t-w}\right)\right.\\ &\left.+[2-(N_i/N)]\left[\frac{1}{(w+1)^2}+\frac{1}{(t-w)^2}\right]+\frac{\ln t}{N(w+1)}\frac{df(w)}{dw}\right\}\end{aligned} \tag{3.14}$$

where $df(w)/dw$ is the differential oscillator strength for the target atom and N_i can be defined as:

$$N_i \equiv \int_0^\infty \frac{df(w)}{dw}dw \tag{3.15}$$

Therefore, integrating Eq. 3.14 over all energies, the total ionization cross section for the BED model is [19]:

$$\sigma_i(t) = \frac{S}{t+u+1}\left[D(t)\ln t + \left(2-\frac{N_i}{N}\right)\left(\frac{t-1}{t} - \frac{\ln t}{t+1}\right)\right] \tag{3.16}$$

where

$$D(t) \equiv \frac{1}{N}\int_0^{(t-1)/2} \frac{1}{w+1}\frac{df(w)}{dw}dw \tag{3.17}$$

The asymptotic behavior of Eq. 3.16 agrees with the asymptotic behavior of the Bethe theory, and also is designed to have the correct behavior at low t where the Bethe theory is not. Comparisons between the BED model with other models as well as experimental data and calculations can be seen in Fig. 3-2 and Fig. 3-3. The BED model is of the same form for the total ionization cross section that is used in Project 8's analysis package, Kassiopeia.

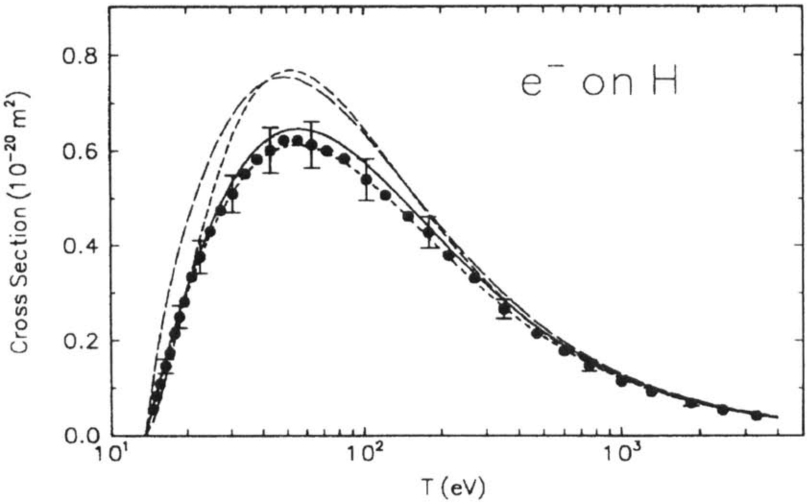

Figure 3-2: The plot shows the total ionization cross section for H by collisions with electrons [19]. The solid line shows the BED model and the points are experimental data conducted by Shah *et al.* [26]. The medium-dashed line shows Gryzinski's cross section [23, 24, 25] and the long-dashed line shows the Born cross section with the electron exchange correction by Younger [27].

3.3 Hydrogen Scattering

3.3.1 Total Scattering Cross Section

For collisions between relativistic charged particles and H_2, the total inelastic cross section is given by [14]:

$$\sigma_{inelastic} = \frac{4\pi a_0^2 z^2}{T/R}\left\{M_{tot}^2\left[\ln\frac{\beta^2}{1-\beta^2}-\beta^2\right]+C_{tot}\right\} \tag{3.18}$$

where $T = \frac{1}{2}m_e v^2$, v is the velocity of the incident particle, m_e is the mass of an electron, a_0 is the Bohr radius, z is the charge of the incident particle, R is the Rydberg energy, c is the speed of light, and $\beta = v/c$. $M_{tot}^2 = (1/3a_0^2)\left\langle(\overrightarrow{r_1}+\overrightarrow{r_2})^2\right\rangle$ and $C_{tot}^2 = M_{tot}^2 \times (\ln c_{tot} + 11.2268)$. $\overrightarrow{r_1}$ and $\overrightarrow{r_2}$ are the position operators of electron 1 and 2. $\left\langle(\overrightarrow{r_1}+\overrightarrow{r_2})^2\right\rangle$ is the expectation value of the wavefunction. The most accurate value

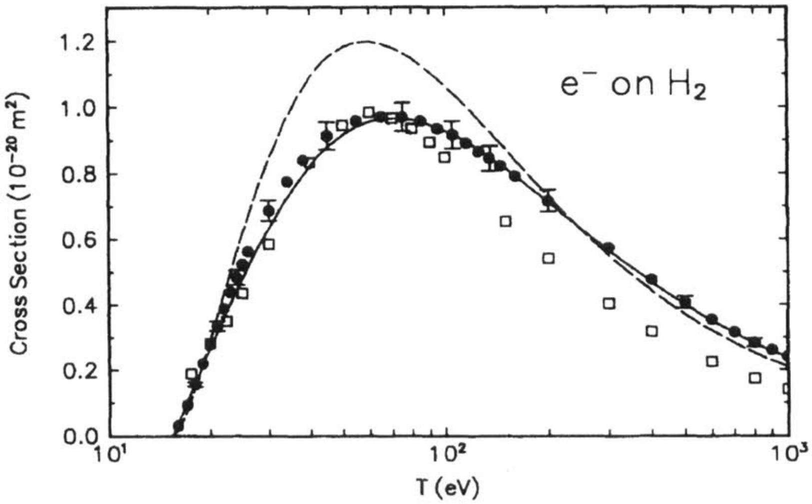

Figure 3-3: The plot shows the total ionization cross section of H_2 by electron collisions [19]. The circles are experimental data from Rapp and Englander-Golden [28] and the squares are calculations by Schultz *et al.* [29]. The solid line is the BED model and the long-dashed line is Gryzinski's cross section [23, 24, 25].

for M^2_{tot} and C^2_{tot} is calculated by Kolos and Wolniewicz [30], where $M^2_{tot} = 1.5487$ and $C^2_{tot} = 17.4615 \pm 0.0434$. With these values, the total inelastic cross section for relativistic particles is [14]:

$$\sigma_{inelastic} = \frac{4\pi a_0^2 z^2}{T/R}\left[1.5487 \ln\left(\frac{\beta^2}{1-\beta^2}\right) + (17.4615 \pm 0.0434)\right] \tag{3.19}$$

The total inelastic cross section of H_2 with electrons of energy 17.8 keV, 30.4 keV, and 32 keV are $\sigma_{17.8,inelastic} = (3.594 \pm 0.204) \times 10^{-18}$ cm^2, $\sigma_{30.4,inelastic} = (2.238 \pm 0.119) \times 10^{-18}$ cm^2, and $\sigma_{32,inelastic} = (2.138 \pm 0.113) \times 10^{-18}$ cm^2. The total cross section of H_2 for several different processes can be seen in Fig. 3-4. Project 8's analysis package, Kassiopeia, utilizes the cross sections calculated by Eq. 3.19 and the cross sections found in Fig. 3-4 for the simulated hydrogen scattering in the program. The total scattering cross section of H_2 with electrons of energy 17.8 keV, 30.4 keV, and 32 keV are $\sigma_{17.8,tot} = 4.446 \times 10^{-18}$ cm^2, $\sigma_{30.4,tot} = 2.856 \times 10^{-18}$ cm^2, and $\sigma_{32,tot} = 2.740 \times 10^{-18}$ cm^2. These values include the ionization cross section [19], elastic scattering [14, 18], electron excitation [16], B-state excitation [17], and other sub-dominant excitations processes. These values will be used to compare to

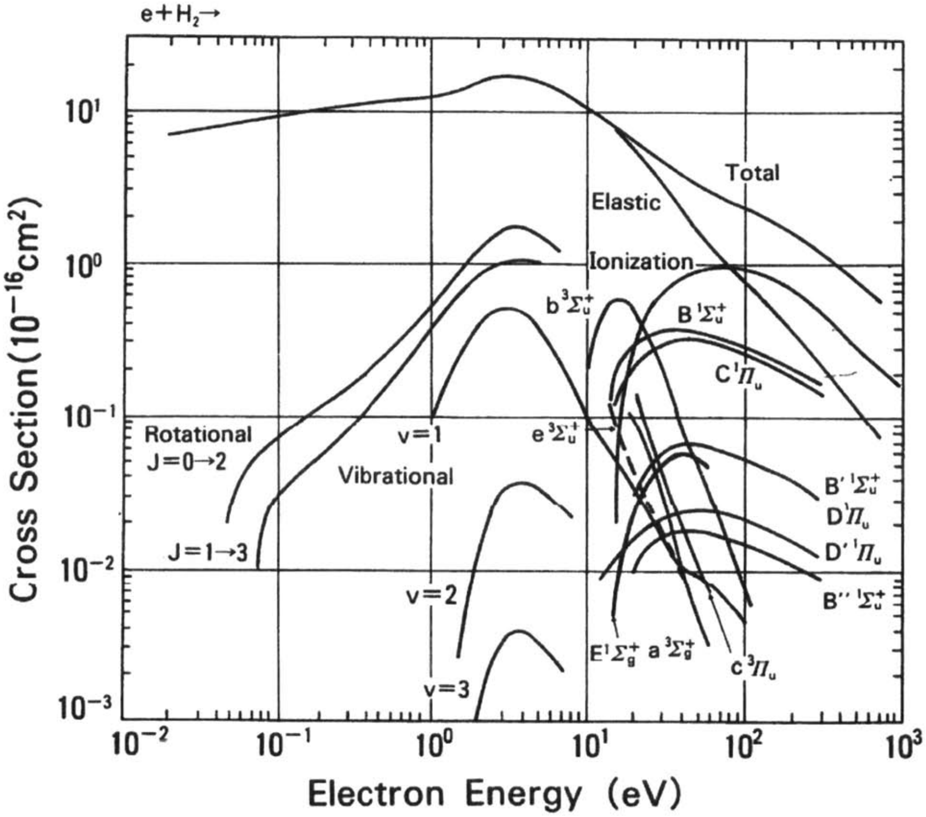

Figure 3-4: A variety of cross sections for H_2, which includes the ionization of atomic hydrogen [31].

the simulations of electron-hydrogen scattering.

3.3.2 Energy Loss

When scattering with atomic hydrogen, electrons lose energy. The kinetic energy of the electron before the collision with atomic hydrogen will be greater than the kinetic energy of the electron after the collision. This energy loss is primarily due to ionization. Ionization occurs when an electron is removed or added to an atom. When an electron with initial kinetic energy, K_i, collides with H_2, the electron will transfer energy to the atom. The energy transferred is the amount of energy required to remove an electron from the atom. This is known as the ionization energy, E_i. The resultant electron has a kinetic energy that is equal to $K_f = K_i - E_i$. The energy loss spectrum can be calculated and observed. It will be shown in Section 6.2.

Chapter 4

Description of the Data and Simulations

4.1 Data Set

The data set that was used for this analysis was taken on June 27, 2014. The experiment was set up to collect electron events stemming from the 17.8 keV and 30.4 keV emission peaks from krypton decay. A plot of the candidate start frequencies is shown in Fig. 4-1. The 17.8 keV peak is between 25.30 GHz and 25.60 GHz. This corresponds to local oscillator frequencies between 1050 MHz and 1350 MHz. The 30.4 keV peak is between 24.70 GHz and 25.05 GHz. This corresponds to local oscillator frequencies of 450 MHz and 800 MHz. Data was taken between these frequencies at 50 MHz intervals (450:50:800 MHz and 1050:50:1350 MHz). The current of the trap coil ranged from 0.8 A to 2.0 A at 0.2 A intervals. At each current, data was taken at all the LO frequencies specified. At each frequency, 10 sec of data was taken in each file, and 10 files were made for each frequency. Because there are 15 frequencies and each frequency had 10 files made, there are 150 data files for each trap current. The approximate amount of time taking data for each trap current was 25 minutes.

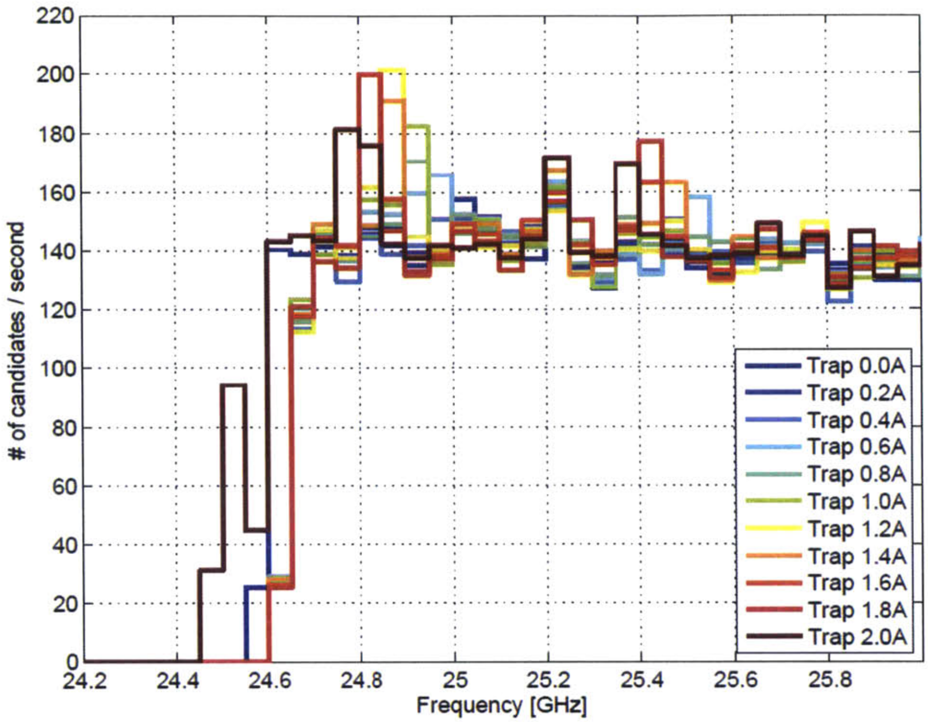

Figure 4-1: A plot of the candidate start frequencies. The candidates with an energy of 17.8 keV are evident between 25.30 GHz and 25.60 GHz. The candidates with an energy of 30.4 keV are evident between 24.70 GHz and 25.05 GHz.

4.2 Conditions on Tracks and Events

Before characterizing events, the individual tracks must first be made. A DBSCAN is run to find clusters of high power bins. To be labeled as a track, four or more high power bins must be within .6 ms away from each other and have a frequency difference of at most .15 MHz. In order to include tracks that only increase in frequency, a cut of a minimum slope of 1 is placed on the data. If all these conditions are met, then a track is made. After all of the tracks are made, another DBSCAN is run to find clusters of tracks. There is no limit to how many tracks can be included in an event, but limits are placed on the time between the tracks, as well as the frequency difference between them. The tracks must be within 2.5 ms and have a frequency difference no greater than 20 MHz. If these conditions are met, then an event is made. There are ranges between no events to a few events in each data file taken.

4.3 Simulations

The Monte Carlo simulations that are conducted in this paper are ran in Kassiopeia, a field calculation and particle tracking software package that was originally made for KATRIN simulations. A detailed description of Kassiopeia can be found in [5]. For these Monte Carlo simulations, the overall magnetic field is set at 1 Tesla that points along the z-axis. The trap coil was made using the cylinder tube configuration. The length of the trap coil is 7.62 mm and the radius ranges from 6.5024 mm to 9.6774 mm. The trap coil is oriented such that the center of the trap coil is located at (0,0,0) and the center axis of the trap coil is aligned with the z-axis. The field of the trap coil is created in the simulation by making the trap coil a solenoid. The trap coil solenoid has 61 turns and has a current of 2.0 A. The waveguide is created using the box configuration. The waveguide is oriented in such a way that the length is parallel to the x-axis, the width is parallel to the y-axis, and the height is parallel with the z-axis with the center of the waveguide at (0,0,0). The length is 10.668 mm, the width is 4.318 mm, and the height is 7.62 cm. These are the dimensions expected for a WR-42 waveguide cell. The positioning of the waveguide and trap coil can be seen in Fig. 4-2.

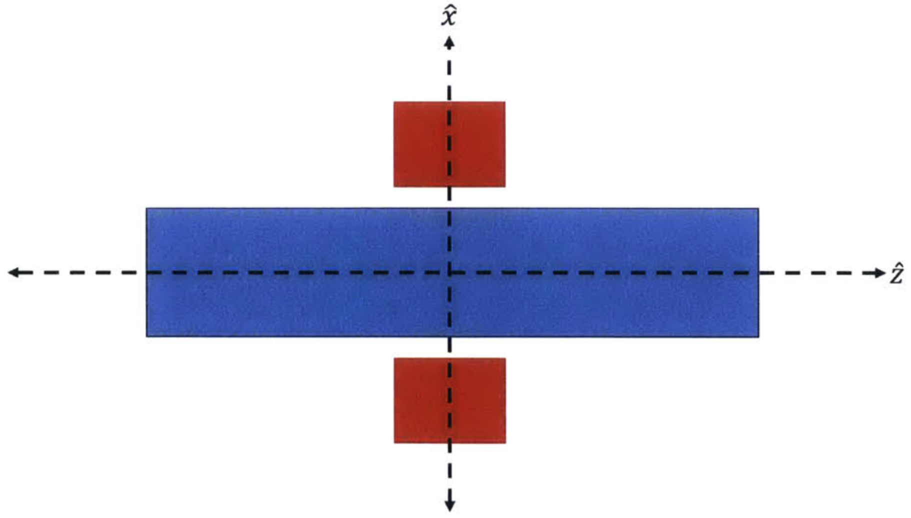

Figure 4-2: A cross section representation of the positioning of the waveguide and trap coil. The rectangular waveguide cross section is shown in blue and the cylindrical trap coil cross section is shown in red.

The events are created in the simulation using a fixed-value generator. Each event starts with a fixed energy in terms of eV that is specified for each run of the simulation. The events have a starting position of (0,0,0). The momentum vector is set with $\theta = 89°$ and $\phi = 90°$ where θ and ϕ are defined by the spherical coordinate system which can be seen in Fig. 4-3. This ensures that the particles will be trapped by the magnetic field. Each event starts out at a time of 0 seconds. The particle's trajectory is calculated using the adiabatic representation, which is an approximation of the exact representation. The difference between the two representations can be seen in Fig. 4-4. Using the adiabatic representation for the particle's trajectory greatly reduces the time it takes for the simulation to finish.

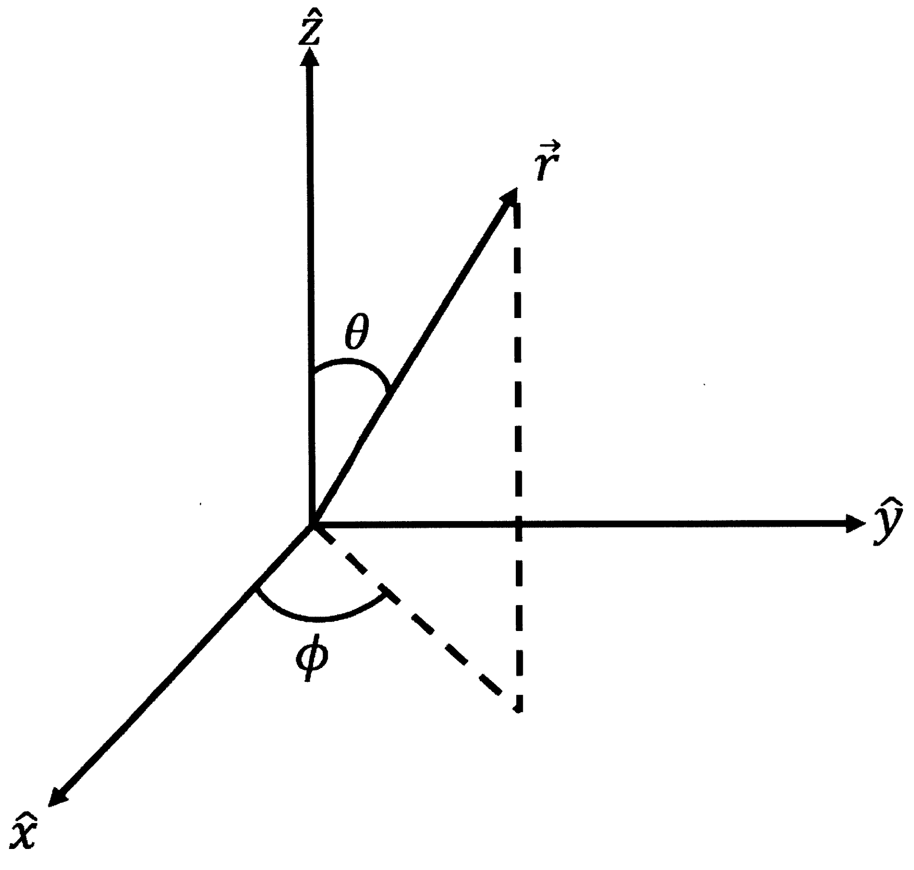

Figure 4-3: An example of the typical spherical coordinate system.

To simulate scattering, gaseous molecular hydrogen is added to the inner volume of the waveguide. Elastic scattering, excitation, and ionization are all included in the simulation. The temperature is set at 300 Kelvin and the pressure is specified for each run of the simulation. A higher pressure was chosen in order to decrease the amount of time the simulations ran. At a pressure of 10 Pa, a simulation took approximately two minutes to complete 50 events. However, at a pressure of 1×10^{-4} Pa, a simulation took approximately three to four weeks to complete 50 events. The density is set to be constant throughout the waveguide. If the initial track of the event scatters off of the hydrogen, a new track is created. This track is still considered to be in the same event as the initial track. The event does not end until one of the terminators have been fulfilled.

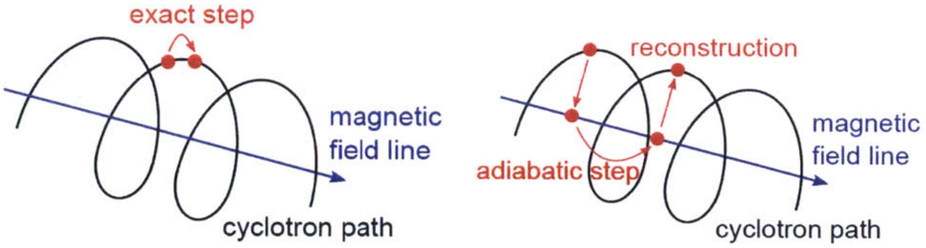

Figure 4-4: The left picture is the exact representation and the right picture is the adiabatic representation [5].

There are three terminators that kill the particles and start a new event if they are fulfilled. The first is if the particle hits the top of the waveguide, the second is if the particle hits the bottom of the waveguide, and the third is if the particle hits any of the side walls of the waveguide. This means that if the particle leaves the waveguide at any side, the event is terminated and a new event begins.

Each simulation has 50 events which corresponds to thousands of tracks. The fixed energy is either 17.8 keV, 30.4 keV, or 32.0 keV. The pressure of the hydrogen gas ranges from 1×10^{1} Pa to 1×10^{-3} Pa. Tracks survive longer as the pressure decreases; therefore the time that each simulation took to finish increased as the pressure decreased.

Chapter 5

Track Length Analysis

5.1 Data

When electrons are released from the decay of krypton, they travel for a certain amount of time before they scatter with hydrogen that is present in the experiment. The amount of time each track survives is measured and recorded. A histogram that is filled with the track times can be fit with an exponential to extract the attenuation time that was discussed in Section 3.1. The equation that is fit to the histogram of track times is:

$$y = e^{p_1 + p_2 t} \tag{5.1}$$

where p_1 and p_2 are the fit parameters and p_2 is the attenuation time. An example of how the attenuation time was extracted from the track time histogram can be seen in Fig. 5-1. The exponential fit of the data does not include a few bins in the beginning of the histogram due to the minimum track length cuts that are made during the initial analysis of the data.

As discussed in the previous chapter, data was taken at specific trap currents. The data at each LO frequency was taken at a specific trap current before moving on to the next trap current. In order to determine if the experiment was relatively stable over the period of data taking, the attenuation time at each current was extracted. A plot of the attenuation time at each current as well as time since the beginning

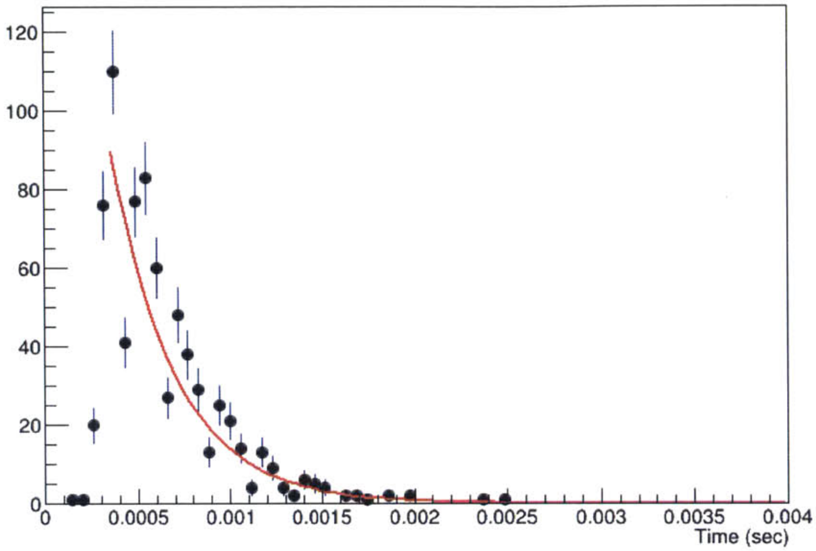

Figure 5-1: The track times when the trap current was 2.0 A are shown in the histogram. An exponential fit using Eq. 5.1 is shown by the red line. For the fit shown, $p_1 = 5.557 \pm 0.101$ and $p_2 = -2.943 \pm 0.138 \times 10^3$ 1/s.

of the data taking period is shown in Fig. 5-2. The plot shows that the experiment remained relatively stable over the period of data taking. The attenuation time averaged over all of the currents is $\mu_t = -2.851 \pm .02897 \times 10^3\ \mathrm{s}^{-1}$. The attenuation time remains essentially unchanged across different trapping currents, providing a systematic uncertainty on the temporal variation of about 1%. Since the experiment remained stable when taking data at the different specified trap currents, the data for all of the currents can be analyzed together for the 17.8 keV peak and the 30.4 keV peak.

When plotting the attenuation time against the energy of the electron, a linear fit of the following form is used:

$$y = p_0 + p_1 x \tag{5.2}$$

where p_0 and p_1 are the fit parameters. The plot of attenuation time versus the energy can be seen in Fig. 5-3. The fit gives the relationship between the attenuation time and the energy for the data:

$$\mu_t = \left(0.05554 \pm 0.005966\ \frac{\mathrm{eV}}{\mathrm{s}}\right) K + \left(-4423 \pm 171.7\ \mathrm{s}^{-1}\right) \tag{5.3}$$

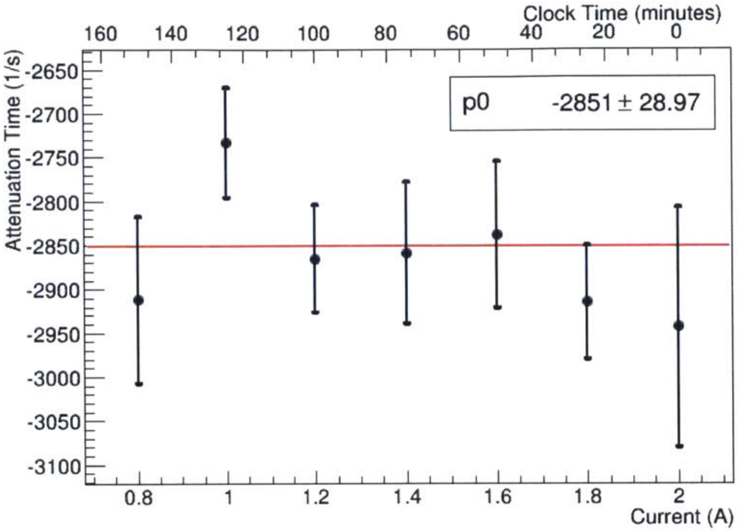

Figure 5-2: A plot of attenuation time versus trap current and clock time. Clock time represents the time since the data taking period began.

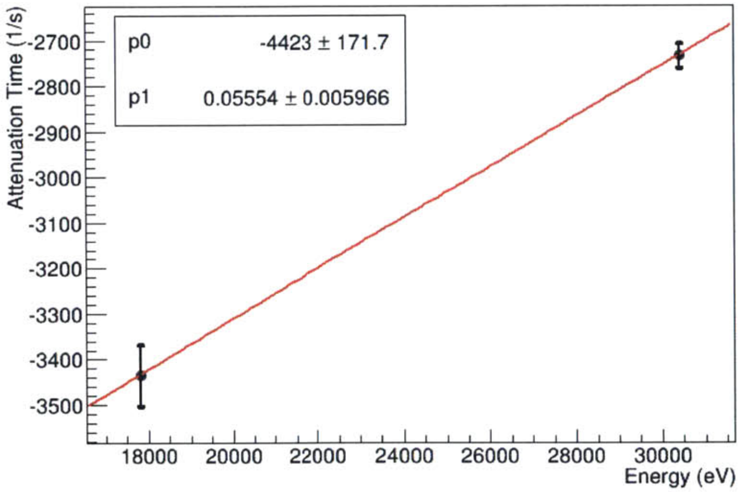

Figure 5-3: A plot of attenuation time versus energy for the data.

5.2 Simulation

The simulations that were ran were described in the previous chapter. For each simulation, a histogram was filled with the time each track survived. The track time histogram was fit with Eq. 5.1 and the attenuation time was extracted. An example of the track time histogram is shown in Fig. 5-4. Since the simulation does not require a particle to surpass a minimum survival time before it is called a track, the track times begin at zero seconds.

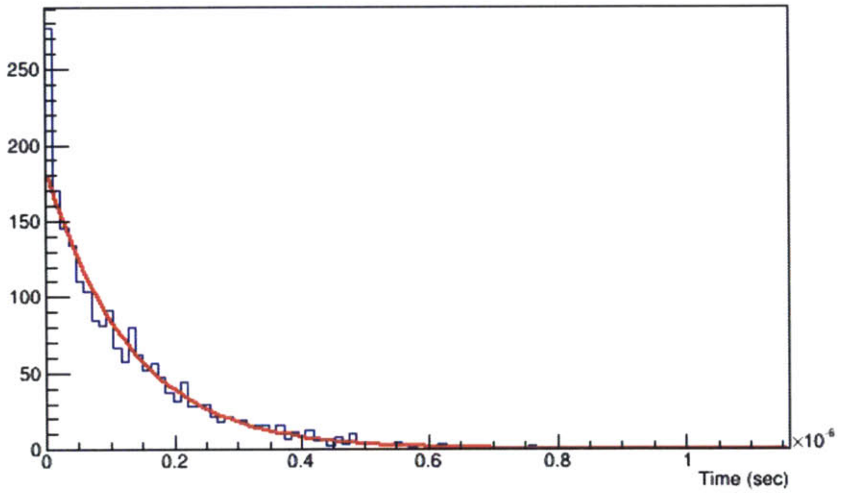

Figure 5-4: The track times when the pressure was 1 Pa are shown in the histogram. An exponential fit using Eq. 5.1 is shown by the red line. For the fit shown, $p_1 = 5.22482 \pm 0.0339$ and $p_2 = -7.805 \pm 0.204 \times 10^6$ 1/s.

The attenuation time was extracted for simulations with a pressure ranging from 1×10^1 Pa to 1×10^{-3} Pa for energies of 17.8 keV, 30.4 keV, and 32.0 keV. The plots of pressure versus attenuation time for the simulations can be seen in Fig. 5-5. The plots are fit with Eq. 5.2. At each energy, the order of magnitude of the attenuation time decreases by a factor of ten as the pressure decreases by a factor of ten. However, the value of the attenuation time stays the same. This shows that increasing or decreasing the pressure for a specific energy does not change the value of the total cross section.

When changing the pressure, the number density and the time a track survives

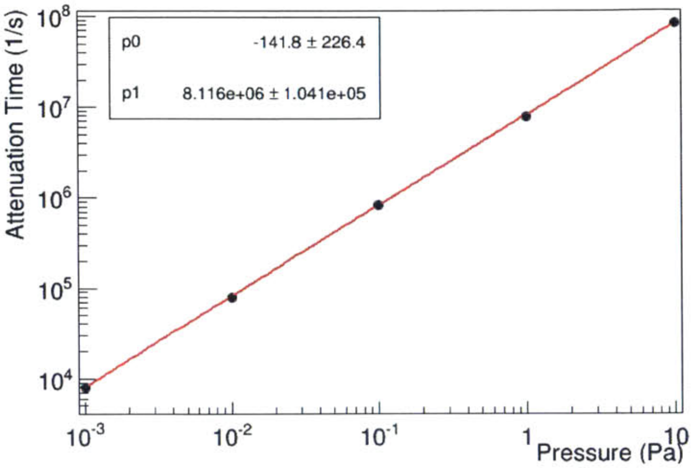

(a) Pressure versus Attenuation Time for 17.8 keV electrons.

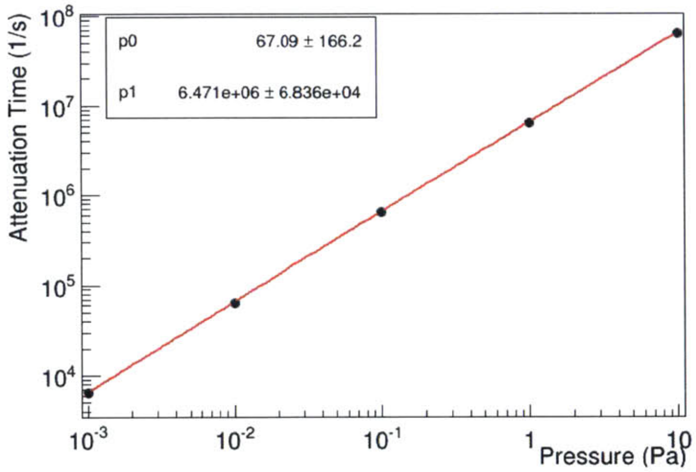

(b) Pressure versus Attenuation Time for 30.4 keV electrons.

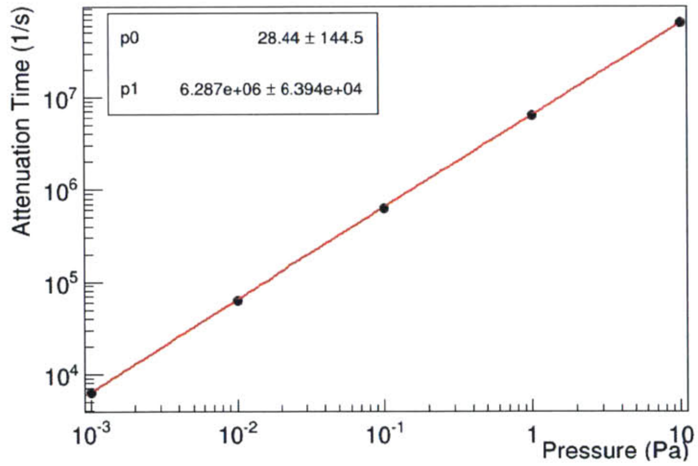

(c) Pressure versus Attenuation Time for 32.0 keV electrons.

Figure 5-5

are affected, but not the cross section. However, the cross section does change with respect to the energy of the incident electron. This can also be seen in Fig. 5-5. Each plot has a different energy for the incident electron. This results in the overall value of the attenuation time to be different. An example of how the attenuation time changes based on what energy the incident electron has can be seen in Fig 5-6.

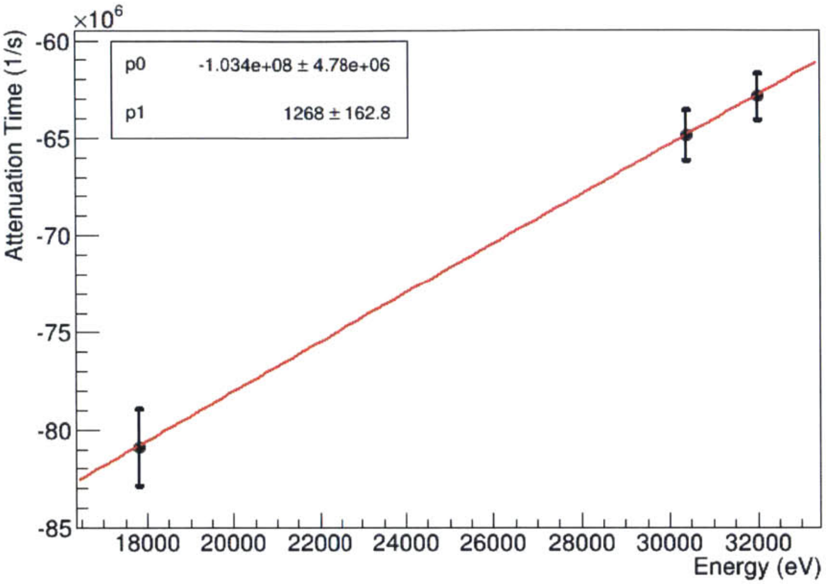

Figure 5-6: Attenuation time versus the energy, where the attenuation time was the average attenuation time over all pressures for each energy.

5.3 Results

The temperature and pressure for the experiment are not extracted with good accuracy. To avoid using those values, $n\sigma$ will be calculated instead of σ for the data. The value of $n\sigma$ for the data can be calculated by manipulating Eq. 3.6:

$$n\sigma = \frac{\mu_t}{v} = \frac{\mu_t}{\beta c} \tag{5.4}$$

The values of $n\sigma$ for the data at the energies of 17.8 keV and 30.4 keV are shown in Table 5.1. Since n is the same for each energy, it is possible to compare the values of the ratio of $n\sigma$ at each energy to the ratio of the cross section values for the

Energy (keV)	β	μ_t (10^3 s^{-1})	$n_d\sigma_{E,d}$ (10^{-7} cm^{-1})
17.8	0.2573	-3.435 ± 0.069	4.453 ± 0.090
30.4	0.3304	-2.735 ± 0.030	2.761 ± 0.030

Table 5.1: The values of $n\sigma$ are calculated for the data at the energies of 17.8 keV and 30.4 keV.

simulations at each energy. For the data, the ratio is:

$$\frac{n_d\sigma_{17.8,d}}{n_d\sigma_{30.4,d}} = 1.613 \pm 0.037(\text{stat}) \pm 0.016(\text{sys}) \tag{5.5}$$

This value will be compared to the theoretical values as well as the simulations.

The number density of the simulations can be calculated by the Van der Waals equation [32]:

$$\left(P + \frac{a}{N_A{}^2}n^2\right)\left(V - \frac{bV}{N_A}n\right) = nkVT \tag{5.6}$$

where P is pressure, n is the number density, N_A is Avogadro's number, V is volume, k is the Boltzmann constant, T is the temperature, and a and b are values that are specific to the individual gas. For H_2, $a = 2.45 \times 10^{-2}$ Pa·m^3 and $b = 2.661 \times 10^{-5}$ mol·m^3 [32]. The volume of the gas is the volume of the waveguide, which is 3.51×10^{-6} m^3. The temperature is 300 K and the pressure changes for each simulation by a factor of 10. The values of the number densities at each pressure that simulations are executed at are shown in Table 5.2. To calculate the total scattering cross section at each energy, the average attenuation time must be calculated for each energy. The

Pressure (Pa)	n_s (cm^{-3})
10	2.414×10^{15}
1	2.414×10^{14}
.1	2.414×10^{13}
.01	2.414×10^{12}
.001	2.414×10^{11}

Table 5.2: The number densities for the simulations calculated using Eq. 5.6.

values of σ for the simulations can be calculated by manipulating Eq. 3.6:

$$\sigma = \frac{\mu_t}{nv} = \frac{\mu_t}{n\beta c} \tag{5.7}$$

Using $n = 2.414 \times 10^{15}$ cm^{-3}, the total scattering cross sections for the simulations are shown in Table 5.3. Using the values in Table 5.3, the ratio of the cross sections

Energy (keV)	β	$\mu_{t,avg}$ (10^7 s^{-1})	$\sigma_{E,s}$ (10^{-18} cm^2)
17.8	0.2573	-8.087 ± 0.201	4.343 ± 0.108
30.4	0.3304	-6.486 ± 0.137	2.712 ± 0.057
32.0	0.3382	-6.287 ± 0.126	2.569 ± 0.051

Table 5.3: The values of σ are calculated for the simulations at the energies of 17.8 keV, 30.4 keV, and 32.0 keV.

at 17.8 keV and 30.4 keV is:

$$\frac{\sigma_{17.8,s}}{\sigma_{30.4,s}} = 1.601 \pm 0.052(\text{stat}) \pm 0.016(\text{sys}) \tag{5.8}$$

where the systematic uncertainty originates from the use of 17.8 keV instead of the true value of 17.83 keV. Using the total theoretical cross section values calculated in Section 3.3, the theoretical ratio for the total scattering cross section is:

$$\frac{\sigma_{17.8,tot}}{\sigma_{30.4,tot}} = 1.557 \tag{5.9}$$

Using the inelastic theoretical cross section values calculated in Section 3.3, the theoretical ratio for the inelastic scattering cross section is:

$$\frac{\sigma_{17.8,in}}{\sigma_{30.4,in}} = 1.606 \pm 0.125 \tag{5.10}$$

The value of the ratio for the simulations is within 2% of its value from the total theoretical ratio. The data ratio is within 4% of its value from the total theoretical ratio. Both the data and the simulation ratios are approximately equal to the ratio of the theoretical inelastic cross section ratio. Since the values of the data and the simulations are approximately equal, the total scattering cross section values for the simulations can be used to calculate the number density of the data. The equation to calculate the number density of the data is:

$$n_d = \frac{n_d \sigma_{E,d}}{\sigma_{E,s}} \tag{5.11}$$

where $n_d \sigma_{E,d}$ are the values that are shown in Table 5.1 and $\sigma_{E,s}$ are the values that are shown in Table 5.3 for the energies (E) of 17.8 keV and 30.4 keV. The number density at 17.8 keV is $(1.025 \pm .033) \times 10^{11}$ cm^{-3} and the number density at 30.4 keV is $(1.018 \pm .024) \times 10^{11}$ cm^{-3}. By taking the average of the two values at 17.8 keV and 30.4 keV, the final number density for the data is $n_d = (1.022 \pm .020) \times 10^{11}$ cm^{-3}. If the temperature of the experiment during data taking was 100 Kelvin, this number density would correspond to a pressure of $(1.411 \pm 0.028) \times 10^{-4}$ Pa.

Chapter 6

Frequency Jump Analysis

6.1 Data

When a particle scatters, there is a change in frequency which corresponds to a loss in energy and/or change in transverse momentum. To calculate this change in frequency, the initial and final frequencies for each track are measured. The frequency difference is then calculated between two tracks, except when the track is the last track of an event. Frequency differences are only calculated between tracks of the same event. The calculation of the frequency difference is:

$$\Delta F = F_{S,n+1} - F_{F,n} \tag{6.1}$$

where $F_{F,n}$ is the final frequency of track n and $F_{S,n+1}$ is the start frequency of track $n+1$. This equation only works until n is the last track of an event. This ensures that the frequency difference for tracks of different events are calculated. An example of a histogram that is filled with the values of the frequency differences for the data is shown in Fig. 6-1.

Histograms of the frequency differences were made for all of the trap currents that the data was taken at. The histograms were then compared to each other in order to see if the peak spread out more as the current changed. The comparison of the histograms at each current is shown in Fig. 6-2. The normalized plot shows that the

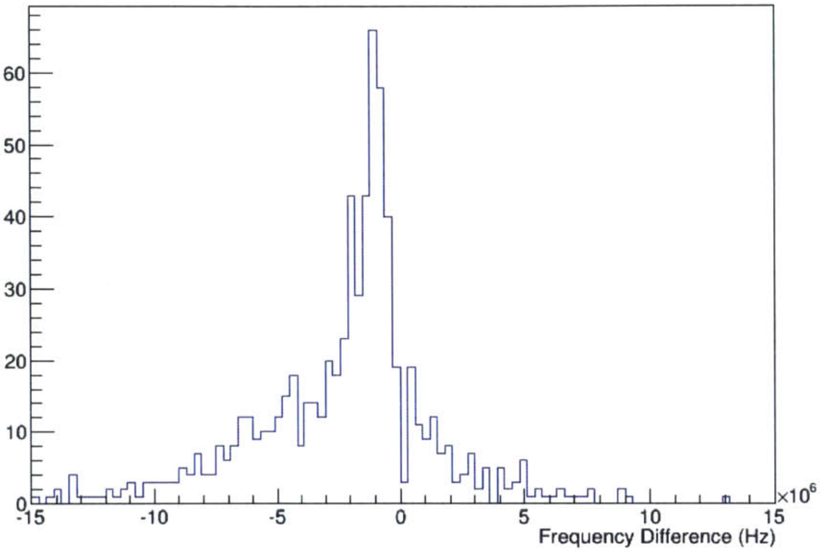

Figure 6-1: The calculated frequency differences for the data set at a trap current of 2 A.

histograms of the frequency differences at each current are statistically similar. The width of the peaks at each current are approximately the same. This allows for the combination of the data to make one histogram for each energy peak. The frequency differences for the 17.8 keV peak and the 30.4 keV can be seen in Fig. 6-3. The dip near zero in each of the histograms could be from the lack of resolution to see extremely small frequency changes due to electron-hydrogen elastic scattering. If the track n undergoes elastic scattering and track $n + 1$ has an initial frequency that is extremely close to the final frequency of track n, then the frequency difference is too small to observe. This could cause the dip near zero that is evident in the plots in Fig. 6-3.

6.2 Simulations

When plotting the electron energy versus time for a simulation, the energy loss when the particle scatters can be clearly seen and the energy loss can be calculated. An example of the kinetic energy of the electron versus time can be seen in Fig. 6-4. To

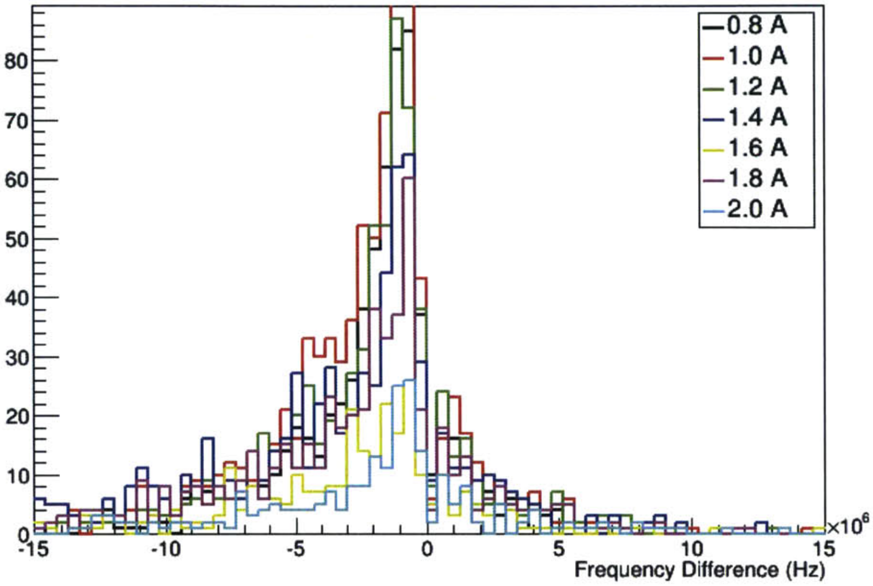

(a) Frequency differences at each current of the data set.

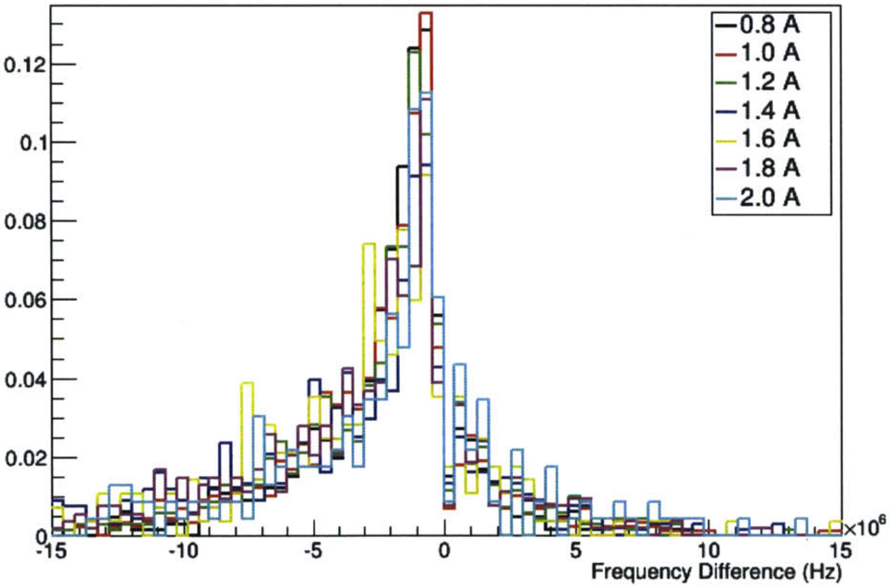

(b) Normalized histograms of frequency differences at each current of the data set.

Figure 6-2

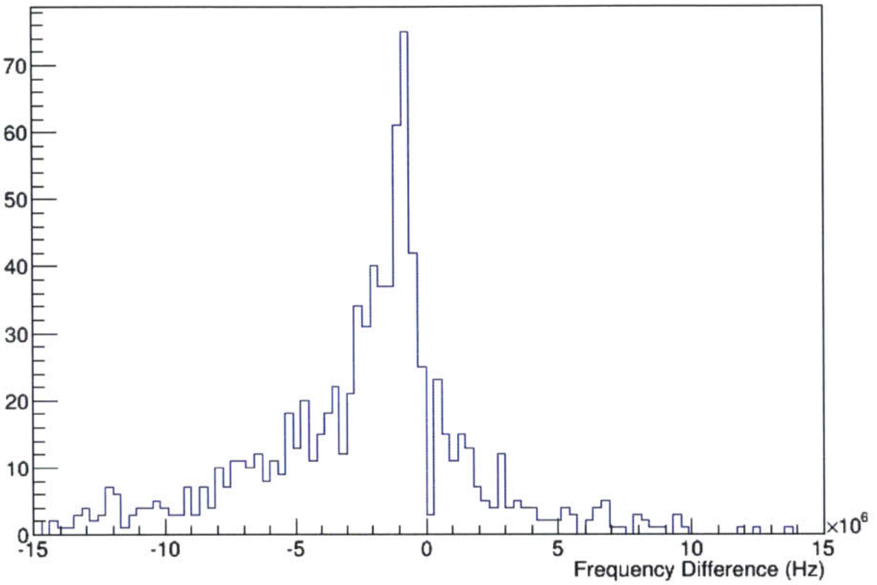

(a) The calculated frequency differences for the data set at every trap current for the energy peak of 17.8 keV.

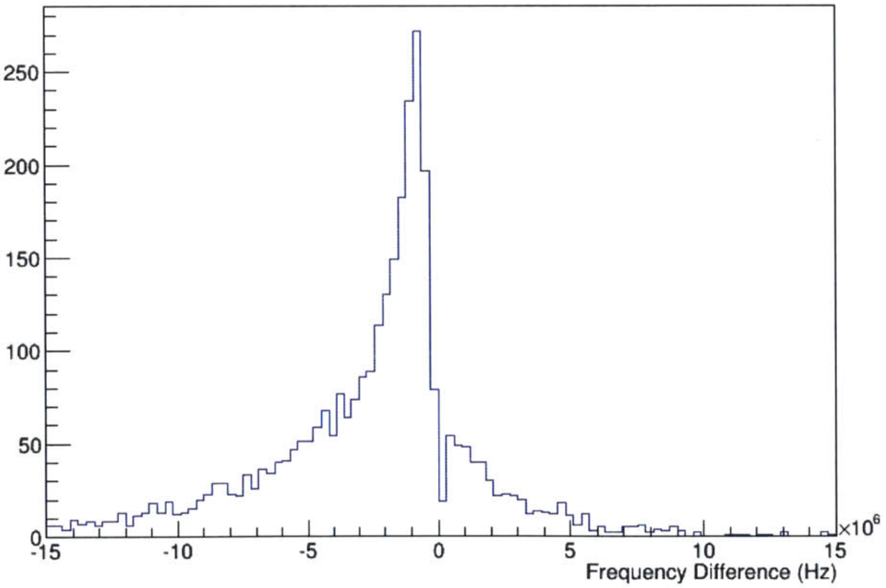

(b) The calculated frequency differences for the data set at every trap current for the energy peak of 30.4 keV.

Figure 6-3

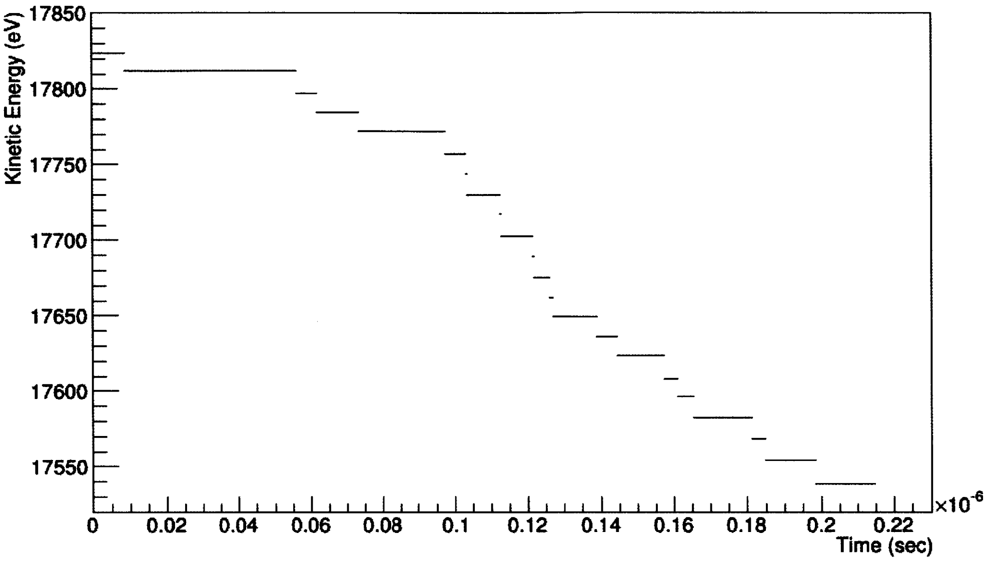

Figure 6-4: The particle loses energy each time it scatters. This simulation has one event. Each line is a single track, and a new track starts when the particle scatters. The energy differences between the tracks is the energy loss.

calculate the kinetic energy difference between two tracks, the initial and final kinetic energy is extracted. The energy difference can then be calculated by:

$$\Delta E = E_{I,n+1} - E_{F,n} \tag{6.2}$$

where $E_{F,n}$ is the final kinetic energy of track n and $E_{I,n+1}$ is the initial kinetic energy of track $n+1$. The energy difference, ΔE, is not calculated if track n is the final track of an event. This avoids calculating the energy difference between tracks of different events.

The simulation calculates the initial and final kinetic energy of each track; however, it does not calculate the observable frequency that we measure in the experiment. The initial and final frequencies of each track must be calculated before the frequency differences can be calculated. The observable frequencies are calculated by:

$$f = \frac{1}{2\pi} \frac{eBc^2}{K + m_e c^2} \left(1 + \frac{\cot^2\theta}{2}\right) \tag{6.3}$$

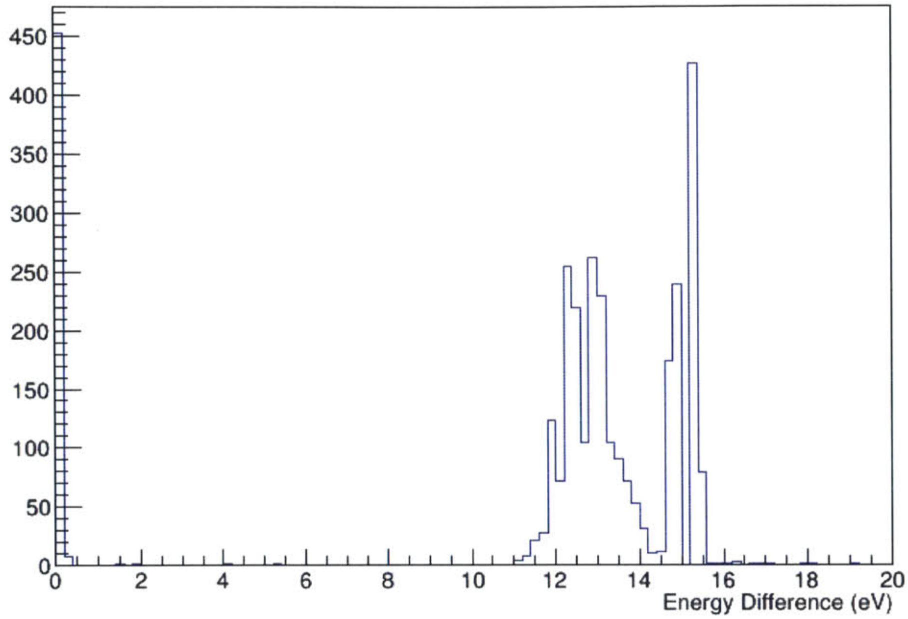

Figure 6-5: The energy loss from electron-hydrogen scattering simulation.

where e is the electron charge, B is the magnetic field strength, m_e is the mass of the electron, c is the speed of light, K is the kinetic energy, and θ is the angle the momentum vector makes with the direction of the magnetic field. To calculate the initial frequency of the track (f_i), the initial kinetic energy of the track is used. To calculate the final frequency of the track (f_f), the final kinetic energy of the track is used. The values that are used for the magnetic field are calibrated using the track frequencies for the data. The initial frequency for first track in each event in the data is plotted based on what the trap current was for that track. Each plot of the track frequencies for each trap current and energy (17.8 keV and 30.4 keV) is fit to extract the peak mean and shape. The peak means are used to calculate the magnetic field. The equation that is fit to the track frequency versus trap current plots in Fig. 6-6 is [34]:

$$f = \frac{q}{2\pi m\left(\frac{K}{511\ \text{MeV}} + 1\right)}\left(B_m - B_t\right) \tag{6.4}$$

where q is the electron charge, m is the electron mass, K is the kinetic energy of the electron, B_m is the magnetic field of the magnet, and B_t is the magnetic field of the

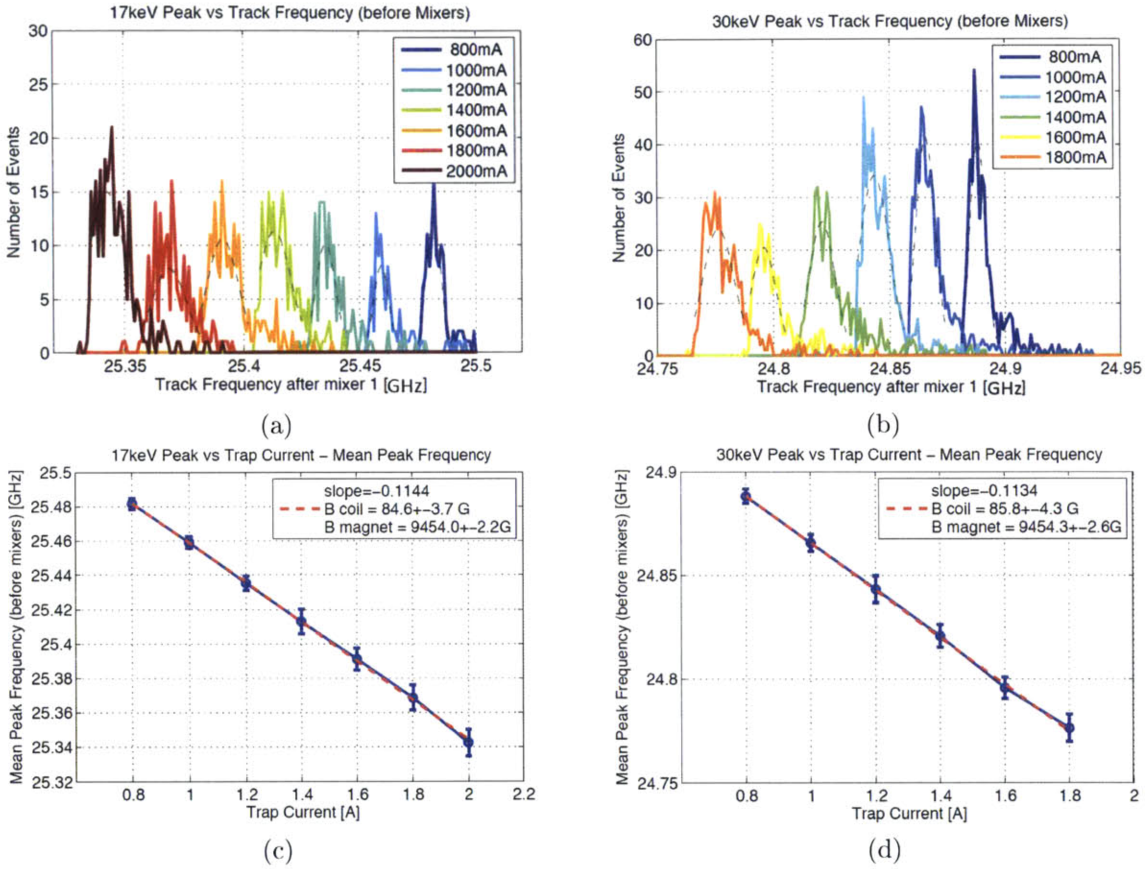

(a) (b)

(c) (d)

Figure 6-6: Figures (a) and (b) are histograms of the initial frequencies for the initial track in each event [33]. Figure (a) has electrons from the 17.8 keV peak and Figure (b) has electrons from the 30.4 keV peak. Each of the individual peaks in each plot is fit to extract the peak mean and shape. Figures (c) and (d) are the peak means versus trap current. Figure (c) has electrons from the 17.8 keV peak and Figure (d) has electrons from the 30.4 keV peak. Figures (c) and (d) are fit with Eq. 6.4 to extract the magnetic field of the magnet and of the trap coil at 2 A.

trap coil. B_t can be represented as [34]:

$$B_t = \frac{I_t}{I_{t,max}} B_{t,max} \tag{6.5}$$

where I_t is the current of the trap coil, $I_{t,max} = 2$ A, and $B_{t,max}$ is the maximum magnetic field of the trap coil at 2 A. By fitting Eq. 6.4 to the frequency versus trap current plots in Fig. 6-6, B_m and $B_{t,max}$ are extracted for the energies of 17.8 keV and 30.4 keV. By averaging the values for B_m and $B_{t,max}$ at each energy, the magnetic field of the magnet is $B_m = 9454.1 \pm 1.7$ G and the maximum trap coil field at 2 A is $B_{t,max} = 85.1 \pm 2.8$ G. Using these two values, the total magnetic field for each run can be calculated by:

$$B_{tot} = B_m - B_t = B_m - \left(\frac{I_t}{I_{t,max}} B_{t,max} \right) \tag{6.6}$$

Once the observable frequencies are calculated using the magnetic field values calculated by Eq. 6.6, the frequency differences for the simulations are calculated by Eq. 6.1. A histogram is filled with these values. An example is shown in Fig. 6-7.

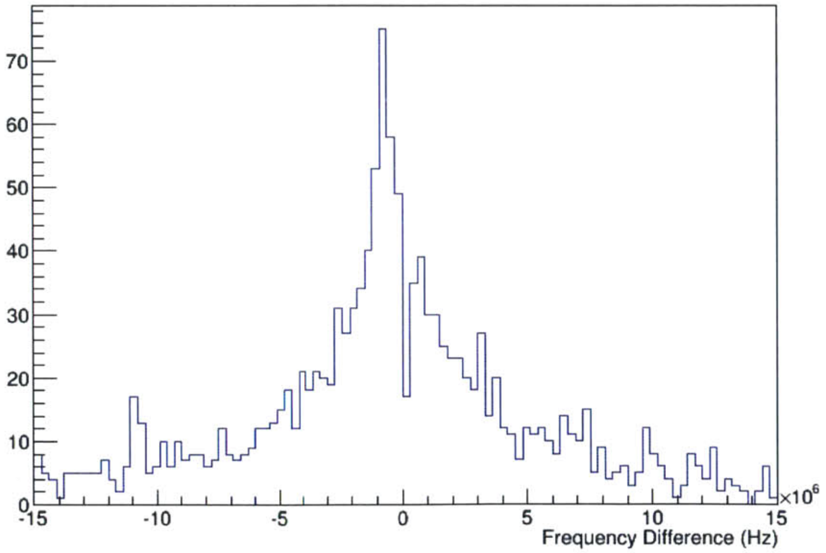

Figure 6-7: A plot of the frequency differences between tracks of the same event for the energy of 17.8 keV.

6.3 Results

In order to see if the physics in the simulations are producing results similar to the data, the initial frequencies of the data and simulations are compared at the energies of 17.8 keV and 30.4 keV. The comparisons can be seen in Fig. 6-8. The start frequencies for the data and the simulations are similar in shape and value. The simulations seem to have good models for cyclotron radiation.

The frequency difference plots are fitted with a Lorentzian function. The particular Lorentzian that is used is split in two, where the two sides meet at the mean of the Lorentzian. Then the two sides of the Lorentzian are raised to separate powers in order to provide the asymmetry that is evident in the frequency difference plots. The original Lorentzian function is:

$$L(x) = \frac{A}{1 + \left(\frac{x-\mu}{\Gamma}\right)^2} \tag{6.7}$$

where A is the amplitude, μ is the mean of the peak, and Γ is the half-width, half-max of the peak. The Lorentzian is symmetric about μ. Since there is asymmetry about μ, an asymmetric Lorentzian is needed. The equation that is fit to the frequency difference plots is:

$$L(x) = \begin{cases} A\left[1 + \left(\frac{x-\mu}{\Gamma}\right)^2\right]^{-\alpha} & x < \mu \\ A\left[1 + \left(\frac{x-\mu}{\Gamma}\right)^2\right]^{-\beta} & x > \mu \end{cases}$$

where α and β are the asymmetry parameters for the left and right side of the Lorentzian. The fits using the asymmetry Lorentzian are shown in Fig. 6-9. The parameters, μ and Γ, are shown in Table 6.1. These results show that the data is more asymmetric than the simulations. Due to the more symmetrical shape of the simulations, the mean of the asymmetrical Lorentzian for the simulations is slightly shifted to the right. The half-width, half-max of the simulations is also larger than that of the data because the data is more asymmetrical. This can also be seen in the plots in Fig. 6-10. The plots compare the frequency difference plots of the data and simulations at the energies of 17.8 keV and 30.4 keV. In the plots, it can easily be

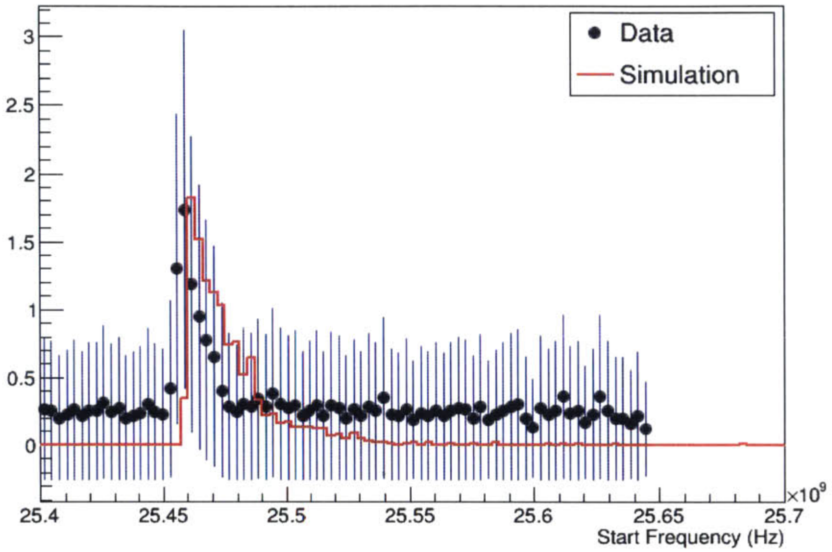

(a) The start frequencies of each track in the simulation with energies of 17.8 keV and a trap current of 1 A.

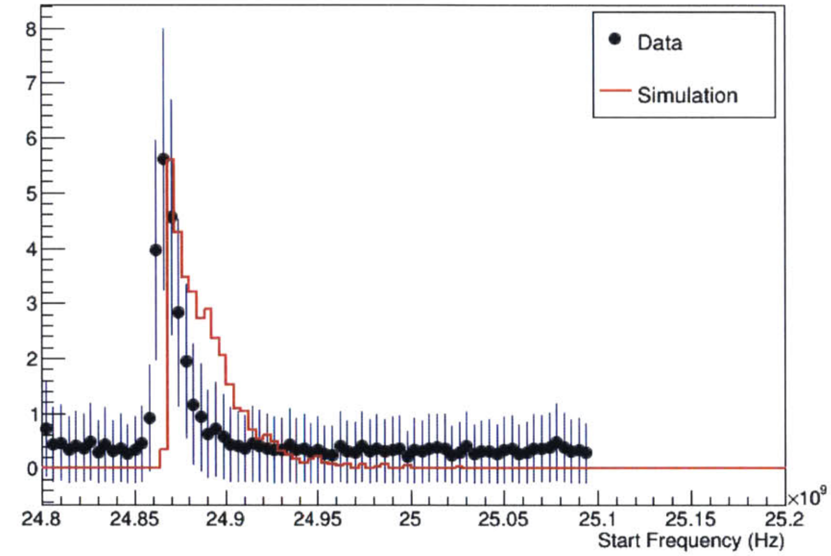

(b) The start frequencies of each track in the simulation with energies of 30.4 keV and a trap current of 1 A.

Figure 6-8

Energy (keV)	Type	μ (MHz)	Γ (MHz)	Γ_α (MHz)	Γ_β (MHz)
17.8	Data	-1.36 ± 0.19	0.74 ± 0.19	1.27 ± 0.35	0.96 ± 0.26
17.8	Sim	-0.58 ± 0.16	2.15 ± 0.44	2.88 ± 0.67	2.82 ± 0.67
30.4	Data	-1.07 ± 0.05	0.59 ± 0.07	1.03 ± 0.13	0.70 ± 0.09
30.4	Sim	-0.83 ± 0.11	1.6 ± 0.36	2.54 ± 0.63	2.61 ± 0.64

Table 6.1: The μ and Γ parameters in the asymmetrical Lorentzian equation for the data and simulations at the energies of 17.8 keV and 30.4 keV. Γ_α and Γ_β are the half-width, half-maximums for each side of the asymmetrical Lorentzian.

seen that the simulations are not as asymmetric as the data; however, the mean of each appear to be approximately the same. To see if the lack of asymmetry is due to how the particle are generated in the simulations, more simulations were run with the particles being generated at any space within the waveguide and with any direction of the momentum vector. The comparisons of the data and the new simulations are shown in Fig. 6-11. The simulations are more asymmetric than when the particles were generated at the center of the waveguide with a fixed angle; however; these simulations are still more symmetric than the data.

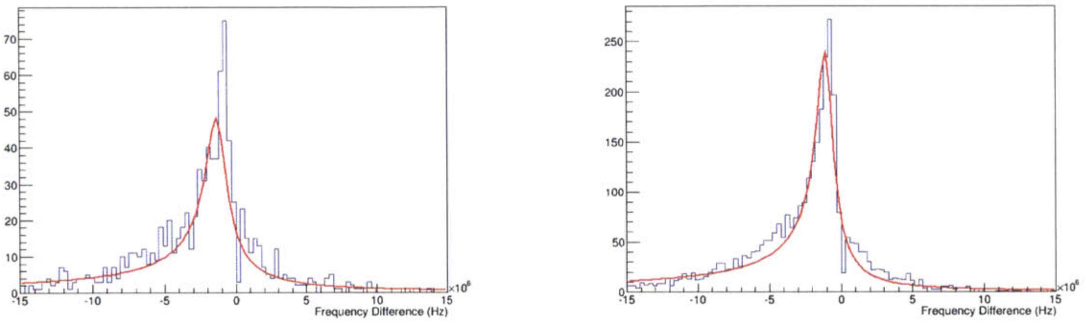

(a) Frequenciy differences for the data at 17.8 keV.

(b) Frequenciy differences for the data at 30.4 keV.

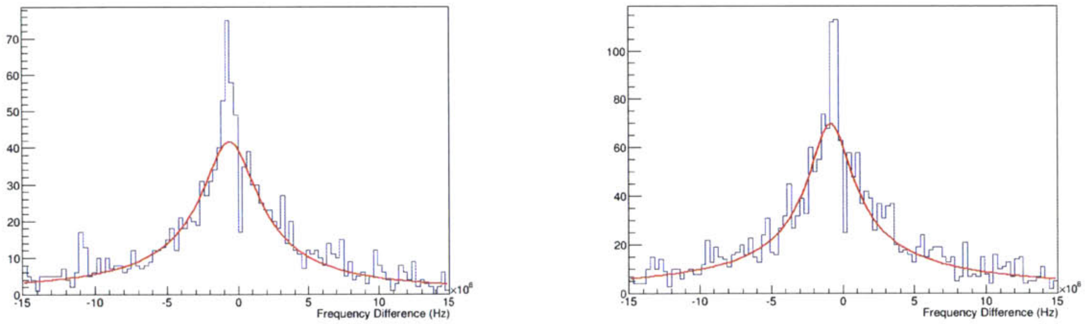

(c) Frequenciy differences for the simulations at 17.8 keV.

(d) Frequenciy differences for the simulations at 30.4 keV.

Figure 6-9

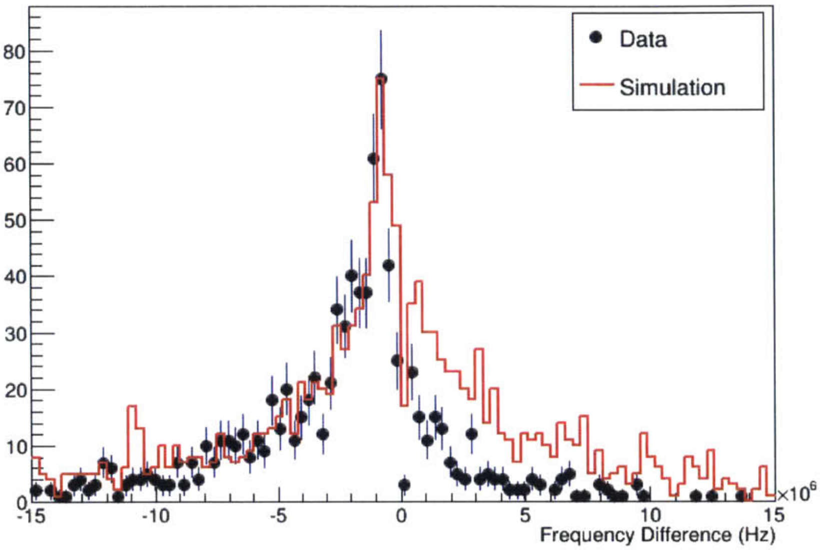

(a) Comparison of the frequency differences for the data and the simulations at 17.8 keV. The simulation had a pressure of 10 Pa. The data included all of the trap currents and the respective LO frequencies for the 17.8 keV peak.

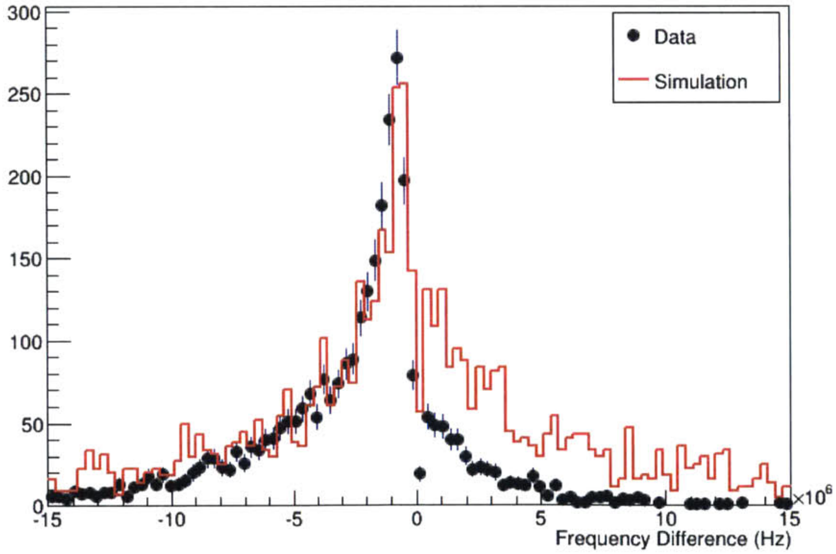

(b) Comparison of the frequency differences for the data and the simulations at 30.4 keV. The simulation had a pressure of 10 Pa. The data included all of the trap currents and the respective LO frequencies for the 30.4 keV peak.

Figure 6-10

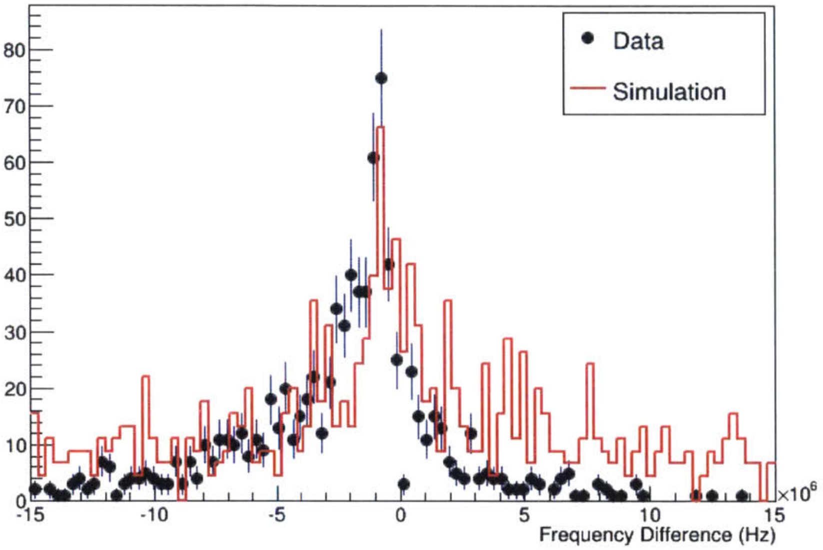

(a) Comparison of the frequency differences at 17.8 keV for the data and the simulations where the particles are generated at any space within the waveguide and with any direction of the momentum vector.

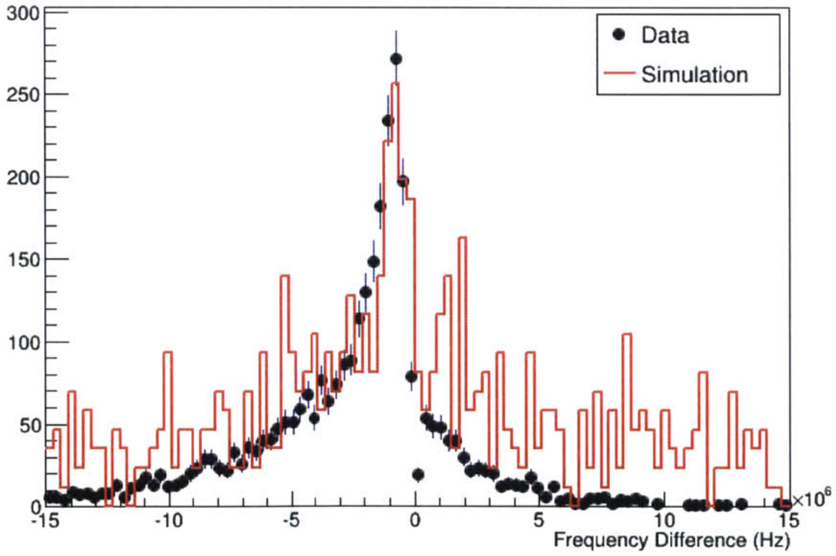

(b) Comparison of the frequency differences at 30.4 keV for the data and the simulations where the particles are generated at any space within the waveguide and with any direction of the momentum vector.

Figure 6-11

Chapter 7

Conclusions

The scattering cross section was calculated using the attenuation time of the tracks for data and simulations. The results of the scattering cross sections, as well as the total and inelastic theoretical values can be seen in Table 7.1. A ratio of the cross sections at 17.8 keV and 30.4 keV were also calculated for the simulations, the total theoretical cross sections, and the inelastic theoretical cross sections:

Energy (keV)	σ_{tot} (10^{-18} cm^2)	σ_{in} (10^{-18} cm^2)	σ_s (10^{-18} cm^2)
17.8	4.446	3.594 ± 0.204	4.343 ± 0.108
30.4	2.856	2.238 ± 0.119	2.712 ± 0.057
32.0	2.740	2.138 ± 0.113	2.569 ± 0.051

Table 7.1: The values of the theoretical total cross section (σ_{tot}), the theoretical inelastic cross section (σ_{in}), and the total cross section of the simulations (σ_s).

$$\text{Ratio} = \frac{\sigma_{17.8}}{\sigma_{30.4}} \tag{7.1}$$

For the data, the ratio included the number density because the number density is not well known for the experiment:

$$\text{Ratio} = \frac{n\sigma_{17.8}}{n\sigma_{30.4}} \tag{7.2}$$

The values of the ratios of the cross sections at the energies of 17.8 keV and 30.4 keV are shown in Table 7.2. The values of the ratios are all within 1σ of each other.

Ratio	Value
Data	$1.613 \pm 0.037(\text{stat}) \pm 0.016(\text{sys})$
Simulations	$1.601 \pm 0.052(\text{stat}) \pm 0.016(\text{sys})$
Total	1.557
Inelastic	1.606 ± 0.125

Table 7.2: The values of the ratios of for the data (Data), the simulations (Simulations), the total theoretical values (Total), and the inelastic theoretical values (Inelastic).

Because of this, the number density was approximated for the data using the values of the cross sections for the simulations. The approximate number density for the data is $n_d = (1.022 \pm .020) \times 10^{11}$ cm^{-3}. If the temperature of the experiment during the period of data taking was 100 Kelvin, this number density would correspond to a pressure of $(1.411 \pm 0.028) \times 10^{-4}$ Pa.

In the frequency versus time plot for the data in Fig. 2-6, jumps in the frequency are evident between the tracks. The frequency jumps were analyzed, and were found to be due to electron-hydrogen scattering. The frequency jumps in the simulations were converted to energy losses. These energy losses can be seen in Fig. 6-5. The peak near 0 eV is from elastic scattering and the peak between 12 eV and 14 eV is from ionization. The frequency difference plots of the data and the simulations have similar structures. They both produce plots that have approximately the same mean; however the asymmetry of the data is more pronounced than the simulations. This can be due to a few reasons. There may be bias in the event reconstruction for the data. The simulation may have a poor scattering model. Also, the data may have better resolution than the simulations. This difference between frequency difference plots for the simulations and the data will be the center of future investigations.

Project 8 presents new techniques to measure the energy of these electrons. We are able to extract the energy and make in-situ cross section measurements. Project 8 will be progressing towards the stage in the experiment where tritium will be introduced in the near future. These proven techniques will be utilized to measure the mass of the neutrino through the beta-decay of tritium.

Bibliography

[1] Zuber, K. *Neutrino Physics*, 2012: Boca Raton, FL.

[2] Rodeback, G. and Allen, J. *Neutrino recoils following the cature of orbital electrons in A37*, 1952.

[3] Xing, Z. and Zhou, S. *Neutrinos in Particle Physics, Astronomy and Cosmology*, 2011: Hangzhou, China.

[4] Drexlin, G. et al. *Current Direct Neutrino Mass Experiments*, 2013.

[5] Furse, Daniel L. *Techniques for Direct Neutrino Mass Measurement Utilizing Tritium Beta-Decay*, 2015.

[6] Asner, D.M. et al. *Single electron detection and spectroscopy via relativistic cyclotron radiation*, 2015.

[7] Herlach, F. and Miura, N. *High Magnetic Fields: Science and Technology*, 2003: New Jersey.

[8] Walker, J. *Fast Fourier Transforms*, 1996.

[9] Frigo, M. and Johnson, S. *FFTW*, 2003.

[10] Weinheimer, Ch. *KATRIN, a next generation tritium β decay experiment in search for the absolute neutrino mass scale*, 2001.

[11] Blaum, K. et al. *The Electron Capture ^{163}Ho Experiment ECHo*, 2013.

[12] Alpert, B. et al. *HOLMES-The Electron Capture Decay of 163Ho to Measure the Electron Neutrino Mass with sub-eV sensitivity*, 2014.

[13] Formaggio, J. *Project 8: Using Radio-Frequency Techniques to Measure Neutrino Mass*, 2011.

[14] Liu, J. *Total Inelastic Cross Section for Collisions of* H_2 *with Fast Charged Particles*, 1973.

[15] Aseev, V. et al. *Energy loss of 18 keV electrons in gaseous* T_2 *and quench condensed* D_2 *films*, 1999.

[16] Celiberto, R. et al. *Scaling of electron-impact electronic excitation cross sections of vibrationally excited diatomic molecules*, 1996.

[17] Janev, R.K. et al. *Elementary Processes in Hydrogen-Helium Plasmas*, 1987: Berlin, Germany.

[18] Trajmar, S. et al. *Electron Scattering by Molecules Il. Experimental Methods and Data*, 1983.

[19] Kim, Y. and Rudd, E. *Binary-encounter-dipole model for electron-impact ionization*, 1994.

[20] Melissinos, A. *Experiments in Modern Physics*, 1966: San Diego, CA.

[21] Rutherford, E. *The Scattering of* α *and* β *Particles by Matter and the Structure of the Atom*, 1911.

[22] Povh, B. et al. *Particles and Nuclei: An Introduction to the Physical Concepts*, 1995: Berlin, Germany

[23] Gryzinski, M. et al. *Two-Particle Collisions. I. General Relations for Collisions in the Laboratory System*,1965.

[24] Gryzinski, M. et al. *Two-Particle Collisions. II. Coulomb Collisions in the Laboratory System of Coordinates*, 1965.

[25] Gryzinski, M. et al. *Classical Theory of Atomic Collisions. I. Theory of Inelastic Collisions*, 1965.

[26] Shah, M.B. et al. *Pulsed Crossed-Beam Study of the Ionization of Atomic Hydrogen by Electron Impact*, 1987.

[27] Younger, S.M. *Electron Impact Ionization Cross Sections and Rates for Highly Ionized Atoms*, 1981.

[28] Rapp, D. and Englander-Golden, P. *Total Cross Sections for Ionization and Attachment in Gases by Electron Impact*, 1965.

[29] Schultz, D.R. et al. *Classical description and calculation of ionization in collisions of 100 eV electrons and positrons with He and* H_2, 1992.

[30] Kolos, W. and Wolniewicz, L. *Potential-energy curves for the* $X\ {}^1\Sigma_g + b^3\Sigma_u+$, *and* $C^1\Pi_U$ *states of the hydrogen molecule*, 1965.

[31] Tawara, H. et al. *Cross Sections and Related Data for Electron Collisions with Hydrogen Molecules and Molecular Ions*, 1989.

[32] Fishman, P. et al. *Physics for Scientists and Engineers*, 2005: Pearson Prentice Hall.

[33] de Viveiros, L. *Magnetic Field calibration using Katydid-DBSCAN events*, 2014: Project 8 internal report.

[34] de Viveiros, L. *Trap Depth Studies*, 2014: Project 8 internal report.